Design, Fabrication, and Measurement of a Silicon Nitride Optomechanical Crystal

by

Thomas Scott Agnew

A thesis submitted in partial fulfillment of the requirements for the degree of

Master of Science

Department of Physics

University of Alberta

© Thomas Scott Agnew, 2022

Abstract

When a photon experiences a change in momentum of any form, be it being absorbed or reflected from a surface, the photon will exert a force upon that material. This force is called the radiation pressure force [1]. One way that we can harness this radiation pressure force is to couple optical and mechanical systems together to form optomechanical systems [2]. One such optomechanical system is the optomechanical crystal (OMC) [3], which consists of an optical waveguide patterned periodically with holes. By placing a defect, in other words by modifying the shape of the holes, in the center of the pattern we can form an optical cavity between the two end regions of the waveguide. This optical mode within the OMC can then excite a mechanical breathing mode in the center of the waveguide through the radiation pressure force.

Optical fiber networks typically use light with wavelengths in the range of 1260 to 1625 nm (184 to 238 THz) since these wavelengths minimizes optical loss within the fiber [4]. In order for the OMC to be resonant with light of this wavelength the OMC must be of similar size, limiting our geometry to the micrometer scale. Fortunately there exist many different techniques, such as electron beam lithography [5] and reactive ion etching [6], which allow for fabrication of devices this small.

In this work, we describe our methods for designing, fabricating, and measuring an OMC made from silicon nitride. Designing the OMC was done through simulation of the optical and mechanical modes using COMSOL Multiphysics. The OMCs were then fabricated at the NanoFAB Fabrication and Characterization Center at the University of Alberta. Light was coupled into the OMC using a dimpled-tapered fiber setup, then measurements of the optical and mechanical properties were done using either a direct detection scheme or a balanced homodyne phase detection scheme. The final device supported an optical mode at $\lambda_o \approx 1482.55$ nm and a mechanical mode at $\omega_m/2\pi \approx 2.62$ GHz with an optomechanical coupling rate of $g_0/2\pi \approx 98.66$ kHz.

Theory is when you know everything but nothing works.

Practice is when everything works but no one knows why.

In our lab, theory and practice are combined:

nothing works and no one knows why.

- unknown

Acknowledgements

Physics research is difficult, and it is even more difficult without support from family, friends, and colleagues. Thankfully, I had many people to support me throughout my masters. Without them, I would not have accomplished what I did.

I would like to specifically acknowledge the hard work and the help I received from my supervisor John P. Davis. Our group is filled with many ambitious and intelligent people who research topics ranging from superfluid helium, to optomechanical or electromechanical systems, to searching for ultra light dark matter. In order to help his students John needed to learn about all of these fields, and I am happy to say that he did an excellent job. Every conversation that I had with John helped push me closer to my goals, and he gave me that little extra nudge forward when I felt like giving up.

Special thanks also goes out to two previous members of the lab, Hugh Ramp and Callum Doolin. Hugh laid the groundwork for the experimental setup I used to measure my devices. Unfortunately he graduated shortly after I joined the group, but during that time he transferred as much of his knowledge as possible to me and he was always available via email or Zoom call after he left the group. Callum was a huge help when it came to the fabrication of my devices. Like cooking, every fabrication recipe is slightly different, but Callum's fabrication steps were a great jumping off point for me. Eventually, using his steps as reference, I was able to optimize my fabrication steps and create the devices that I measured in this thesis. Additionally, Callum greatly contributed to the institutional knowledge that was used in the lab. In particular, his Resolved Instruments photodetectors with the associated analysis software PteroDAQtyl were used every single day in the lab. It is safe to say that without Hugh and Callum I would of struggled a lot more on this project.

I would also like to thank all the other members of the lab. Often I would approach members of the group with a question that I was struggling with, and regardless of what the other person was doing they would help as much as they could. Through struggling together I can safely say that I made some

lasting friendships during my time here.

Lastly I would like to thank my family and friends back home in Calgary. Every visit to Calgary was filled with fun events, be it going to a pub to watch a hockey game, or doing an escape room, or going rock climbing or skating, etc. Like a battery, these trips recharged my mental and emotional reserves, enabling me to focus back on work when I returned to Edmonton. Being away from home for 3 long years has made me realize just how important my family and friends are to me, and I am very much looking forward to coming back home.

Contents

1 Introduction and Theory **1**
1.1 Introduction 1

2 Optomechanical System Theory **5**
2.1 Optical Cavity Theory 5
2.1.1 Optical Cavity Hamiltonian 6
2.1.2 Input-Output Theory for Optical Cavities 7
2.2 Mechanical Resonator Theory 9
2.2.1 Mechanical Resonator Hamiltonian 9
2.2.2 Input-Output Theory for Mechanical Resonators 10
2.3 Optomechanical Theory 11
2.3.1 Radiation Pressure Force 11
2.3.2 Interaction Hamiltonian 12
2.3.3 Rotating Wave Approximation 13
2.3.4 Linearizing the Hamiltonian 13
2.3.5 Coupled Optomechanical Equations of Motion 14

3 Photonic crystal design, simulation, and fabrication **16**
3.1 Crystal Theory 17
3.1.1 Optical Plane Waves 17
3.1.2 Mechanical Plane Waves 20
3.2 Simulations 22
3.2.1 Unit Cell Simulations 22
3.2.2 Full Device Simulations 25
3.3 Fabrication 27
3.3.1 Substrate Cleaning and Preparation 27
3.3.2 Electron Beam Lithography 28
3.3.3 Reactive Ion Etching 31
3.3.4 Wet etching 33
3.3.5 Fabrication Summary 35

4 Measurement Techniques **37**
4.1 Optical Measurement Techniques 37
4.1.1 Dimpled-Tapered Fibers 37
4.1.2 Optical Direct Detection 40
4.2 Mechanical Measurement Techniques 42
4.2.1 Mechanical Direct Detection 43
4.2.2 Homodyne Detection 44
4.2.3 Electrical Downmixing 47
4.2.4 Power Spectral Densities 49
4.3 Experimental Setup and Results 51
4.3.1 Optical Mode Characterization 51
4.3.2 Mechanical Mode Characterization 52

4.3.3 Optomechanical Coupling Rate 54

5 Conclusion **59**
5.1 Summary 59
5.2 Next Steps 60

Bibliography **62**

List of Tables

3.1 Al RIE recipe used in this thesis. This is the nanofabs standard recipe for etching Al [47]. Adjustments to the etching steps process time can be made depending on the thickness of the Al layer. 31
3.2 SiN RIE recipe used in this thesis. This etch recipe was given to me by my colleague Elham Zohari [50]. Adjustments to the etching steps process time can be made depending on the thickness of the SiN layer. 32

5.1 Summary of the optical and mechanical properties of the OMC measured in this thesis 60

List of Figures

1.1 A simple schematic of an optomechanical system. Two mirrors separated by a distance L together form an optical cavity, and the light within the cavity has frequency ω_{c}. The mirror on the right is connected to a spring, such that the radiation pressure force from the light within the cavity will cause this mirror to move. The interaction between this force and the restoring force of the spring will cause the mirror to oscillate mechanically at frequency ω_{m}. 2

3.1 A) A schematic of how light rays refract at the interface of two materials with index n_1 and n_2. The parallel component of the wavevectors of the two light rays must be conserved, from which one can derive Snell's law. B) An example of a band diagram for a waveguide. The light line ($\omega = ck_{\|}$) is shown in red. Above this line there is a continuous spectrum of modes called the light cone, and below this line there is discrete spectrum of modes called index guided modes. C) Example of a waveguide periodically patterned with holes which will exhibit discrete translational symmetry. Each hole is separated by a distance a, such that the system is unchanged when moving up or down the waveguide in steps of na where $n \in \mathbb{Z}$. 19

3.2 Examples of the unit cell geometry used in our COMSOL simulations. A) Unit cell geometry with labels for the unit cell width (a), the ellipse semi-axes (hx and hy), and the width of the waveguide. The unitcell also has a thickness t, but this is not shown in this figure. Figures B-D show the geometry of the unit cell and air box used for the optical simulation. The blue shaded regions are B) the PML layer, C) the periodic boundary condition, and D) the perfect magnetic conductor boundary condition. E) Geometry of the unit cell for the mechanics simulation with the periodic boundary condition labeled in blue. Note that the periodic boundary conditions are placed on both the shown surface and the surface opposite the one shown. . . 23

3.3 A) Optical band diagram for our unit cell geometry. The grey region represents the continuum of modes that exist outside the unit cell, while the white region represents index guided modes of the unit cell. The light line $\omega = ck$ separates these two regions. The black lines and blue dot-dashed lines represent modes with different polarizations (see text). The red shaded region is the quasi-bandgap between the lower and upper black bands. The inset shows the simulated electric field profiles for the lower and upper bands labeled with a black line. B) Mechanical band diagram for our unit cell geometry. The black lines and blue dot-dashed lines represent symmetric and non-symmetric modes respectively. Simulated displacement field profiles are shown in the inset for the lower and upper bands respectively. 24
3.4 A) Schematic of our OMC with the mirror regions outlined in blue and the defect region outlined in green. B) Simulated optical mode electric field profile. Notice how the field is confined to the defect region. C) Simulated mechanical mode displacement field profile. Comparing the optical and mechanical modes notice that there is a large amount of spatial overlap between the two modes. 26
3.5 Schematic of how an EBL system works. Taken from [5]. . . . 28
3.6 A) Full device geometry and B) hole geometry for the GDSII files used in this thesis. The bulk area around the waveguide drawn in green is patterned using straight or curved lines while the holes are patterned using a dot-dose array. The colour of the dots corresponds to the dose that dot receives, with red dots receiving a higher dose while blue dots receive a lower dose. . 29
3.7 The above plot is taken from [49]. This plot compares the dose needed to fully develop the exposed electron beam resist (dose to clear) to the temperature of the developer used. When taking this data the authors submerged the chips in the developer for 10 s. The four square data points represent their four separate trials, while the blue dashed curve is a fit to their data points. 30
3.8 Example of how KOH etches Si along the $< 111 >$ crystal axis, leading to features with an angle of 54.7° when etching Si with a $< 100 >$ crystal orientation. Image taken from [53]. 33
3.9 A) A collection of various liquids with their associated critical temperatures and pressures taken from [55]. B) Phase diagram for CO_2 taken from [54]. 34
3.10 A) A flow chart briefly summarizing the steps required for fabricating the OMCs used in this thesis. More details can be found within the text. B) Scanning electron microscope image of one of the OMCs fabricated for this thesis. 36

4.1 A) A Schematic of the fiber after being tapered, adapted from a similar schematic in reference [57]. d_0 is the initial width of the fiber, d_w is the final width of the fiber, l_t is the length of the tapered region, and l_h is the region of fiber exposed to the hydrogen flame. B) Optical microscope image of a completed dimpled-tapered fiber. 39

4.2 A) Example of a Lorentzian shaped transmission dip, such as the ones we expect to observe when measuring the optical resonance of the OMC. The optical resonance is located at the bottom of the Lorentzian, and the total coupling rate is the full-width-half-max of the resonance. B) Microscope image of coupling a dimpled-tapered fiber to an OMC. C) Schematic of how light is coupled into and out of the optomechanical crystal. 41
4.3 A) When the optical mode is modulated by the mechanical signal, it will cause the optical resonance to oscillate back and forth. This $d\omega$ is shown by the gray sinusoid. When doing mechanical direct detection, the laser is detuned from the resonance to the point on the optical resonance with the steepest slope. This translates the change in cavity resonance into a change in transmission detected on the photodiode, dT. The phase of the optical mode is similarly modulated by the mechanical signal, as shown by the grey sinusoid in figure B). In this case, the laser is kept tuned to the optical resonance since this is the point with steepest slope. Information about the mechanical mode is encoded in $d\theta$. 43
4.4 A simple schematic of how an IQ mixer works. The RF and LO signals are sent to two mixers, one of which has had the LO signal phase shifted by 90°, allowing access to both quadratures of the mixed signal. 48
4.5 A) A schematic of the experimental setup used in this thesis. The optical paths are drawn using a red line while the electronic paths are drawn in black. Beam splitters are denoted using a black line angled at 45°, polarization controllers are denoted using 3 sequential circles, and the optical switch is denoted using three red dots oriented in a triangle. Note that the beam splitter right after the laser is a variable beam splitter, allowing for adjusting the ratio of light in the local oscillator and device arms. The various electronic and optical components are as follows: EOM = electro-optic modulator, FS = fiber stretcher, OMC = optomechanical crystal, BPD = balanced photodiode, IQ = IQ mixer, LO = local oscillator. B) A photo of the fiber setup used in this thesis. Note that an additional polarization controller and EOM have been added to the local oscillator arm, allowing for also doing heterodyne measurements. 50
4.6 A) A plot comparing the coupling distance to the shape of the optical transmission. More details are shown by comparing the coupling distance to B) the total, intrinsic and extrinsic coupling rates, and C) optical resonance wavelength. 52
4.7 A) PSD of the mechanical resonance of our OMC for an input laser power of 10 mW. Also shown here is a fit to the data, from which we obtain $Q_\mathrm{m} = 2126$ and $\Gamma_\mathrm{m} = 1.23$ MHz. B) PSD for various laser powers, showing the power dependence of our mechanical signal. C) Simultaneous measurement of the mechanical PSD and the optical resonance, showing the relationship between laser wavelength and mechanical signal amplitude. . . 53
4.8 A) Example of a frequency spectrum of an EOM. Adapted from a figure taken from [66]. B) The amplitudes of the carrier and first side band of the EOM are fit to the first two squared Bessel functions. The point where $\beta_\mathrm{EOM} = \pi$ is used to calibrate the V_π of the EOM. 57

Chapter 1

Introduction and Theory

1.1 Introduction

Today it is well known that light has wave-particle duality, meaning that it displays properties of both waves and particles, but before this became common knowledge one of the greatest battles in physics was the debate to determine whether light was a particle or a wave. This battle dates back to research performed by Isaac Newton where he developed his corpuscular theory of light. This theory stated that every source of light emits tiny light particles called corpuscles into the medium surrounding the source and that these corpuscles are perfectly elastic, rigid, and weightless [7]. The main problem with this theory was that it did not account for properties of light such as refraction and diffraction. Other theories that proposed the wave nature of light, such as those proposed by contemporary physicists René Descartes [8], Robert Hook [9], and Christiaan Huygens [10], were able to explain these properties of light, but they were greatly overshadowed by the popularity of Newton's Corpuscular theory. It wasn't until the interference and diffraction properties of light were clearly demonstrated in the famous double slit experiments by Thomas Young in the early 19th century that wave models became widely accepted [11].

No theories were able to account for all properties of light, and so research continued. It wasn't until 1900, through his study of black-body radiation [12], that Max Planck discovered that electromagnetic energy was not absorbed or emitted from a system continuously, but is absorbed or emitted in discrete

chunks. In other words, electromagnetic energy is quantized and can only be added or removed from a system in integer multiples of the energy quantum $E = \hbar\omega$ where ω is the angular frequency of light and $\hbar = h/2\pi$ is the reduced Planck's constant. Following this, Albert Einstein showed that if light energy is quantized then its momentum must also be quantized [1], leading to the idea of the photon with momentum quantum $p = \frac{\hbar\omega}{c}$ where c is the speed of light.

Cavity optomechanics is one field continuing to study the properties of light [2]. Pictured in Fig. 1.1 is a simple schematic of an optomechanical system consisting of two mirrors separated by a distance L where one mirror is attached to a mechanical element such as a spring. The light within the optical cavity is called resonant if it forms a standing wave between the two mirrors, in other words, if $\omega_\mathrm{c} = m\pi\frac{c}{L}$ where $m \in \mathbb{Z}$. We include m in this definition since there is not just a single resonance, but many resonances separated by $\Delta\omega_\mathrm{c} = \pi\frac{c}{L}$. When each photon, carrying momentum $p = \frac{\hbar\omega}{c}$, reflects off the

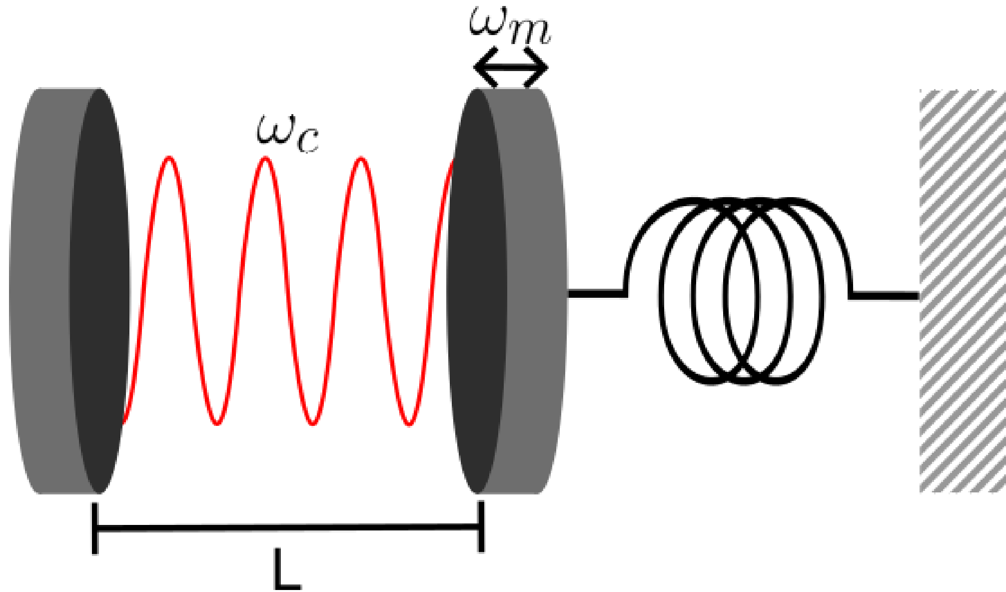

Figure 1.1: A simple schematic of an optomechanical system. Two mirrors separated by a distance L together form an optical cavity, and the light within the cavity has frequency ω_c. The mirror on the right is connected to a spring, such that the radiation pressure force from the light within the cavity will cause this mirror to move. The interaction between this force and the restoring force of the spring will cause the mirror to oscillate mechanically at frequency ω_m.

surface of the mirror it experiences a momentum change $\Delta p = 2\frac{\hbar\omega}{c}$ such that it is now traveling in the opposite direction with the same momentum. Due to conservation of momentum, the mirror must have experienced a force due to this momentum change: the radiation pressure force [1]. For the mirror attached to a spring this force causes the spring to be compressed, increasing the distance between the two mirrors. The light within the cavity is no longer resonant, which reduces the force on the mirror allowing the restoring force of the spring to push the mirror back to its equilibrium position. This will happen repeatedly, causing the mirror to oscillate back and forth with a frequency ω_{m}. This radiation pressure force is the mechanism through which an optical cavity is coupled to a mechanical resonator, and this is the basis for the field of optomechanics.

Optomechanical systems can take many forms, one example of which is the Fabry-Perot cavity with a movable end mirror [13] shown in Fig. 1.1. Other examples of optomechanical systems include trapped atoms [14], whispering gallery mode resonators [15], and optomechanical crystals [16]. One application of such systems is for transducing between different frequencies of light. For example, superconducting qubits typically use GHz photons and operate at millikelvin temperatures [17]. The number of thermal photons within the system is described using the Bose-Einstein distribution [17]:

$$\bar{n}_{\mathrm{th}} = \frac{1}{e^{\hbar\omega/k_B T} - 1}, \tag{1.1}$$

so these low temperatures are required in order to keep the system deep within the thermal groundstate ($\bar{n}_{\mathrm{th}} \ll 1$) and limit the amount of noise added to the system by thermal photons. If one was to try and connect two such systems at room temperature, they would be required to transduce the photons to a higher frequency in order to remain deep within the thermal groundstate.

One proposed method for transducing between optical and GHz photons is through a triply-resonant system [18]. This method would perform the transduction in two steps: first the GHz photons would be transduced to GHz phonons, then these same GHz phonons would be transduced to optical photons. One such system has been built previously in our lab using a

gallium arsenide optomechanical crystal coupled to a 3D microwave cavity [16, 18]. Optical photons were transduced to GHz phonons via the photoelastic effect, and then those phonons were transduced to GHz photons via the piezoelectric effect. The result of this experiment was a single-photon to single-photon transduction efficiency of $\eta \approx 10^{-15}$, which must be increased to tens-of-percent before it will be competitive with classical microwave-to-optical converters [18]. A proposed improvement of this experiment was to repeat this measurement using an optomechanical crystal made from lithium niobate, since this material has stronger piezoelectric properties [18]. This previous work was performed using optomechanical crystals fabricated by one of the groups at NIST, so our group would like to learn how to fabricate optomechanical crystals here at the University of Alberta. Since lithium niobate is expensive, and since our group has little experience fabricating optomechanical crystals, the goal of my research was to design, simulate, and fabricate an optomechanical crystal made from silicon nitride with the goal of eventually transitioning to lithium niobate.

In Chapter 2 we begin by discussing the theory of optical and mechanical resonators both as isolated systems and as a coupled optomechanical system. Following this, in Chapter 3 we go over the methods for designing, simulating, and then fabricating optomechanical crystals from silicon nitride. Chapter 4 will then provide details about the various measurement techniques used to characterize the optical and mechanical properties of an optomechanical system. Finally, chapter 5 will provide a summary of the results of these measurements, as well as a discussion on possible next steps for this research.

Chapter 2

Optomechanical System Theory

This chapter will discuss briefly the theoretical knowledge needed to understand the simulations and experiments performed in later chapters. We begin in section 2.1 by discussing the theory of optical cavities by analogy to the Fabry-Perot cavity. Steady state solutions will be derived from the system Hamiltonian, while state dynamics will be described using input-output theory. This theory will then be repeated for the mechanical motion of the system in Section 2.2. The final section of this chapter will discuss the mechanism by which the optical cavity and mechanical resonator are coupled, as well as deriving the interaction Hamiltonian and the coupled input-output equations of motion. Note that the derivations performed in this chapter are adapted from similar derivations in references [2], [18], [19], and [20].

2.1 Optical Cavity Theory

From Fig. 1.1, consider only the optical cavity formed by the two mirrors separated by a distance L. Inside the cavity, assume light is polarized in the x direction and propagates in the z direction such that it reflects back and forth between the two mirrors. The electric field of this wave can be described using the equation [20]:

$$\mathcal{E}_x(z,t) = \mathcal{E}_0 \sin(kz)\sin(\omega_c t), \tag{2.1}$$

where $\mathcal{E}_{\mathrm{x0}}$ is the amplitude, $k = 2\pi/\lambda$ is the wave vector, and ω_{c} is the cavity frequency. There also exists a magnetic field orthogonal to this electric field that propagates in the same direction. The magnetic field can be described

using the equation [20]:

$$\mathcal{B}_y(z,t) = \mathcal{B}_0 \cos(kz)\cos(\omega_c t), \tag{2.2}$$

where $\mathcal{B}_0 = \mathcal{E}_0/c$ is the amplitude.

2.1.1 Optical Cavity Hamiltonian

The following derivation for the Hamiltonian for light confined in an optical cavity follows the derivation performed in chapter 7 of reference [20]. The energy density for the light trapped in the cavity is given by [20]:

$$U = \frac{1}{2}\left(\epsilon_o \mathcal{E}^2 + \frac{1}{\mu_o}\mathcal{B}^2\right), \tag{2.3}$$

from which we can find the energy stored within the fields by integrating over the length of the cavity. For light that is resonant in the cavity, that is $\lambda = \frac{2L}{m}$ where $m = 1, 2, 3, ...$, the result of this integration is [20]:

$$E(t) = \frac{L}{4}\left(\epsilon_o \mathcal{E}_0^2 \sin^2(\omega_\mathrm{c} t) + \frac{\mathcal{B}_0^2}{\mu_o}\cos^2(\omega_\mathrm{c} t)\right), \tag{2.4}$$

where ω_c is the resonant frequency of the cavity. This can be simplified by introducing a new set of coordinates analogous to the position and momentum [20]:

$$q(t) = \sqrt{\frac{\epsilon_o L}{2\omega_\mathrm{c}^2}}\mathcal{E}_0 \sin(\omega_\mathrm{c} t), \tag{2.5}$$

$$p(t) = \sqrt{\frac{L}{2\mu_o}}\mathcal{B}_0 \cos(\omega_\mathrm{c} t), \tag{2.6}$$

which leads us to rewrite the energy stored in the field as [20]:

$$E(t) = \frac{1}{2}\left(p^2(t) + \omega_\mathrm{c}^2 q^2(t)\right). \tag{2.7}$$

This can be further simplified by making use of second quantization and rewriting the energy in terms of annihilation and creation operators. Recall that the annihilation and creation operators are given by [20]:

$$\hat{a}(t) = \sqrt{\frac{\omega_\mathrm{c}}{2\hbar}}\left(\hat{q}(t) + \frac{i}{\omega_\mathrm{c}}\hat{p}(t)\right), \tag{2.8}$$

$$\hat{a}^\dagger(t) = \sqrt{\frac{\omega_\mathrm{c}}{2\hbar}}\left(\hat{q}(t) - \frac{i}{\omega_\mathrm{c}}\hat{p}(t)\right), \tag{2.9}$$

which conversely means that we can write:

$$\hat{q}(t) = \sqrt{\frac{\hbar}{2\omega_\mathrm{c}}}(\hat{a}^\dagger(t) + \hat{a}(t)), \tag{2.10}$$

$$\hat{p}(t) = i\sqrt{\frac{\hbar\omega_\mathrm{c}}{2}}(\hat{a}^\dagger(t) - \hat{a}(t)). \tag{2.11}$$

Rewriting the energy in terms of the annihilation and creation operators, we arrive at our Hamiltonian [20]:

$$\hat{H}(t) = \hbar\omega_\mathrm{c}(\hat{a}^\dagger(t)\hat{a}(t) + 1/2), \tag{2.12}$$

which describes the steady state solution for light trapped in an optical cavity.

2.1.2 Input-Output Theory for Optical Cavities

Instead of adding terms to the Hamiltonian to describe the dynamics of the system, it is much easier to use either master equations or input-output theory [2]. Master equations are used when only the internal dynamics of the system are of interest, meanwhile if you need to access the light field emitted or reflected by the system you can use input-output theory. In our system we will need to couple light in and out of the system, therefore input-output theory is the best candidate for formulating the physics of our system.

The following derivation is derived following similar derivations in references [2] and [19]. To begin, we need to determine the time evolution of our field, $\hat{a}(t)$. This can be done by using Heisenberg's equation of motion [2, 19]:

$$\dot{\hat{O}} = -\frac{i}{\hbar}[\hat{H}(t), \hat{O}]. \tag{2.13}$$

By replacing $\hat{O}$ with $\hat{a}(t)$ we obtain:

$$\dot{\hat{a}}(t) = -i\omega_\mathrm{c}\hat{a}(t), \tag{2.14}$$

which describes a lossless optical cavity with resonant frequency ω_c. Inputs and outputs can then be added on to the end of this equation. Most notably, there will be a decay rate associated with the cavity corresponding to the reflection coefficient of the mirrors [2]. This can be described as $-\frac{\kappa}{2}\hat{a}(t)$ where κ is the cavity decay rate. κ can be further split into intrinsic, κ_o, and extrinsic, κ_e,

losses, $\kappa = \kappa_\text{o} + \kappa_\text{e}$. Intrinsic losses correspond to the natural decay rate of the cavity, while extrinsic losses correspond to light that is intentionally coupled out of the cavity [2]. Similarly, light that is intentionally coupled into our cavity can be written as $\sqrt{\kappa_\text{e}}\hat{a}_\text{in}(t)$ while any stray light that couples into the cavity can be written as $\sqrt{\kappa_\text{o}}\hat{f}_\text{in}(t)$. $\hat{f}_\text{in}(t)$ is typically assumed to be zero, so adding all these inputs and outputs to Eq. (2.14) we obtain [2]:

$$\dot{\hat{a}}(t) = -i\omega_\text{c}\hat{a}(t) - \frac{\kappa}{2}\hat{a}(t) + \sqrt{\kappa_\text{e}}\hat{a}_\text{in}(t), \tag{2.15}$$

which is the input-output theory equation of motion for an optical cavity.

The amplitude and frequency of the input field will be controlled using an external laser. Typically the amplitude is held constant while the frequency is swept across the optical cavity resonance. This allows us to separate out the time dependence of our fields such that [2]:

$$\hat{a}_\text{in}(t) \rightarrow \hat{a}_\text{in}e^{-i\omega_\text{l}t}, \tag{2.16}$$

$$\hat{a}(t) \rightarrow \hat{a}(t)e^{-i\omega_\text{l}t}. \tag{2.17}$$

Substituting the two fields back into our equation of motion yields [2]:

$$\dot{\hat{a}}(t) = i\Delta\hat{a}(t) - \frac{\kappa}{2}\hat{a}(t) + \sqrt{\kappa_\text{e}}\hat{a}_\text{in}, \tag{2.18}$$

where $\Delta = \omega_\text{l} - \omega_\text{c}$. Notice that for the cavity field, $\hat{a}(t)$, we have explicitly kept the time dependence of the field and only separated out the portion that has frequency ω_l. After substitution, all the $e^{-i\omega_\text{l}t}$ terms cancel out, meaning that we are in a frame that is rotating at the laser frequency. This is called the rotating wave approximation [20], and is useful when we are only concerned with the difference between the cavity and laser frequencies and not with the frequencies themselves.

When the inputs and outputs are balanced, in other words when the field is in its steady state ($\dot{\hat{a}}(t) = 0$), we can determine the average number of photons in the cavity by taking the expectation value of $\hat{a}^\dagger\hat{a}$ [2]. In the steady state,

the field and its complex conjugate are given by [2]:

$$\hat{a} = -\frac{\sqrt{\kappa_{\mathrm{e}}}\hat{a}_{\mathrm{in}}}{\kappa/2 + i\Delta}, \tag{2.19}$$

$$\hat{a}^{\dagger} = -\frac{\sqrt{\kappa_{\mathrm{e}}}\hat{a}_{\mathrm{in}}^{\dagger}}{\kappa/2 - i\Delta}, \tag{2.20}$$

from which we obtain the average number of intracavity photons [2]:

$$\bar{n}_{\mathrm{c}} = \langle \hat{a}^{\dagger}\hat{a} \rangle = \frac{\kappa_{\mathrm{e}}|\hat{a}_{\mathrm{in}}|^2}{\kappa^2/4 + \Delta^2}, \tag{2.21}$$

which will become useful later when we characterize the system.

2.2 Mechanical Resonator Theory

Now, consider attaching a spring to one of the mirrors of our optical cavity. The radiation pressure of the light in the cavity will push on the mirror, causing it to oscillate back and forth. This motion can be described as a driven-damped harmonic oscillator [2]:

$$F_{\mathrm{ext}}(t) = m_{\mathrm{eff}}\frac{d^2x(t)}{dt^2} + m_{\mathrm{eff}}\Gamma_{\mathrm{m}}\frac{dx(t)}{dt} + m_{\mathrm{eff}}\omega_{\mathrm{m}}^2 x(t), \tag{2.22}$$

where m_{eff} is the effective mass of the oscillator, Γ_{m} is the mechanical damping rate, and ω_{m} is the mechanical mode frequency. Solutions for the center of mass displacement will have the form [2]:

$$x(t) = x_0 e^{-\frac{\Gamma_{\mathrm{m}} t}{2}} \cos\left(\sqrt{\omega_{\mathrm{m}}^2 - \frac{\Gamma_{\mathrm{m}}^2}{4}} t\right), \tag{2.23}$$

and can exist in three regimes: underdamped ($\Gamma_{\mathrm{m}}^2 < 4\omega_{\mathrm{m}}^2$), critically damped ($\Gamma_{\mathrm{m}}^2 = 4\omega_{\mathrm{m}}^2$), and overdamped ($\Gamma_{\mathrm{m}}^2 > 4\omega_{\mathrm{m}}^2$). For our application we will be working with an underdamped oscillator, where our oscillation frequency is close to the natural frequency $\omega_{\mathrm{m}} \approx \omega_0 = \sqrt{\frac{k}{m_{\mathrm{eff}}}}$.

2.2.1 Mechanical Resonator Hamiltonian

The following derivation is derived following similar a derivation in reference [18]. The potential and kinetic energy of a harmonic oscillator are given

by [18]:

$$V = \frac{1}{2} m_{\text{eff}} \omega_m^2 x^2, \tag{2.24}$$

$$T = \frac{p^2}{2m_{\text{eff}}}, \tag{2.25}$$

and the classical Hamiltonian of this system is the sum of the total energy in the system [18]:

$$H = \frac{p^2}{2m_{\text{eff}}} + \frac{m_{\text{eff}} \omega_{\text{m}}^2 x^2}{2}. \tag{2.26}$$

Similar to how we treated the optical Hamiltonian, we can move from a classical Hamiltonian to a quantum Hamiltonian by using second quantization. To do this we introduce the phonon annihilation and creation operators [2]:

$$\hat{b}(t) = \frac{1}{2x_{\text{zpf}}} \left(\hat{x}(t) + \frac{i}{m_{\text{eff}} \omega_{\text{m}}} \hat{p}(t) \right), \tag{2.27}$$

$$\hat{b}^\dagger(t) = \frac{1}{2x_{\text{zpf}}} \left(\hat{x}(t) - \frac{i}{m_{\text{eff}} \omega_{\text{m}}} \hat{p}(t) \right), \tag{2.28}$$

or similarly:

$$\hat{x}(t) = x_{\text{zpf}} (\hat{b}(t) + \hat{b}^\dagger(t)), \tag{2.29}$$

$$\hat{p}(t) = -i m_{\text{eff}} \omega_{\text{m}} x_{\text{zpf}} (\hat{b}(t) - \hat{b}^\dagger(t)), \tag{2.30}$$

where:

$$x_{\text{zpf}} = \sqrt{\frac{\hbar}{2m_{\text{eff}} \omega_{\text{m}}}}, \tag{2.31}$$

is the zero point fluctuation amplitude of the mechanical mode. Inserting these annihilation and creation operators into the classical Hamiltonian yields [2]:

$$\hat{H} = \hbar \omega_{\text{m}} (\hat{b}^\dagger \hat{b} + 1/2), \tag{2.32}$$

which is the standard quantum harmonic oscillator Hamiltonian.

2.2.2 Input-Output Theory for Mechanical Resonators

The procedure for deriving the input-output theory equation for a mechanical resonator is very similar to what we did for the optical cavity. This derivation follows a similar derivation found in reference [18]. First, we use Heisenberg's equation to determine the time evolution of our field [18]:

$$\dot{\hat{b}}(t) = -i \omega_{\text{m}} \hat{b}(t), \tag{2.33}$$

which describes a lossless mechanical resonator with a mechanical frequency ω_{m}. Next we need to consider terms for any inputs and outputs [2]. The main output of our system is associated with the mechanical dissipation of the mechanical mode. This is given by the exponential term in Eq. (2.23) and will be added to our equation of motion as $-\frac{\Gamma_{\mathrm{m}}}{2}\hat{b}(t)$ [2]. Similarly, any mechanical signal that is added to the system can be added as $\sqrt{\Gamma_{\mathrm{m}}}\hat{b}_{\mathrm{in}}(t)$ [2]. This leads to the expression [18]:

$$\dot{\hat{b}}(t) = -i\omega_{\mathrm{m}}\hat{b}(t) - \frac{\Gamma_{\mathrm{m}}}{2}\hat{b}(t) + \sqrt{\Gamma_{\mathrm{m}}}\hat{b}_{\mathrm{in}}(t), \tag{2.34}$$

which is the input-output theory equation of motion for our mechanical resonator.

We can also look at the steady state solutions of the mechanical resonator's equation of motion to determine the average number of phonons in the cavity. The steady state solutions are given by [2]:

$$\hat{b}(t) = \frac{\sqrt{\Gamma_{\mathrm{m}}}\hat{b}_{\mathrm{in}}(t)}{\frac{\Gamma_{\mathrm{m}}}{2} - i\omega_{\mathrm{m}}^2}, \tag{2.35}$$

$$\hat{b}^\dagger(t) = \frac{\sqrt{\Gamma_{\mathrm{m}}}\hat{b}_{\mathrm{in}}(t)}{\frac{\Gamma_{\mathrm{m}}}{2} + i\omega_{\mathrm{m}}^2}, \tag{2.36}$$

and we can find the average number of phonons by taking the expectation value $\langle\hat{b}^\dagger\hat{b}\rangle$, giving us the expression [2]:

$$\bar{n}_m = \langle\hat{b}^\dagger\hat{b}\rangle = \frac{\Gamma_{\mathrm{m}}|\hat{b}_{\mathrm{in}}|^2}{\frac{\Gamma_{\mathrm{m}}^2}{4} + \omega_{\mathrm{m}}^2}. \tag{2.37}$$

2.3 Optomechanical Theory

2.3.1 Radiation Pressure Force

As mentioned in Chapter 1, radiation pressure force is the fundamental mechanism that couples the cavity radiation field to the mechanical motion [2]. Recall that due to conservation of momentum, both the photon and mirror of the optical cavity must experience a change in momentum of $\Delta p = 2\frac{\hbar\omega}{c}$. From this, we can derive the radiation pressure force from the expression $F = \frac{\Delta p}{\Delta t}$

where $\Delta t = 2L/c$ is the round-trip time for a Fabry-Perot cavity of length L, and Δp is as defined above. The result is:

$$\langle \hat{F} \rangle = \frac{\hbar\omega_{\mathrm{c}}}{L}\hat{n}_c, \tag{2.38}$$

where $\hat{n}_c = \langle \hat{a}^\dagger, \hat{a} \rangle$ is the average number of photons inside the cavity. It is also convenient to define the frequency pull parameter $G = -\delta\omega_{\mathrm{c}}/\delta x$ which allows us to relate the change in cavity resonance frequency with position [2]. In the case of a Fabry-Perot cavity the frequency pull parameter is $G = \omega_{\mathrm{c}}/L$.

2.3.2 Interaction Hamiltonian

The following derivation is derived following a similar derivation in reference [2]. The Hamiltonian for the uncoupled optical and mechanical modes is given by:

$$\hat{H}_0 = \hbar\omega_{\mathrm{c}}\hat{a}^\dagger\hat{a} + \hbar\omega_{\mathrm{m}}\hat{b}^\dagger\hat{b},$$

where the 1/2 terms have been dropped for simplicity. Since the cavity resonance frequency is modulated by the mechanical amplitude, we can approximate the cavity frequency as the series [2]:

$$\omega_{\mathrm{c}}(x) \approx \omega_{\mathrm{c}} + x\partial\omega_{\mathrm{c}}/\partial x + ... \tag{2.39}$$

The displacement due to radiation pressure is typically small, so truncating to first order is sufficient to approximate the dynamics of the system. Inserting this expression for the cavity frequency back into the optical component of the uncoupled Hamiltonian yields [2]:

$$\hbar\omega_{\mathrm{c}}(x)\hat{a}^\dagger\hat{a} \approx \hbar(\omega_{\mathrm{c}} - G\hat{x})\hat{a}^\dagger\hat{a},$$

but if we recall from Eq. 2.29 that the position is given by $\hat{x} = x_{\mathrm{zpf}}(\hat{b} + \hat{b}^\dagger)$ we arrive at an expression for the interaction Hamiltonian [2]:

$$\hat{H}_{\mathrm{int}} = -\hbar g_0\hat{a}^\dagger\hat{a}(\hat{b} + \hat{b}^\dagger), \tag{2.40}$$

where we have now defined the single-photon optomechanical coupling rate [2]:

$$g_0 = Gx_{\mathrm{zpf}}. \tag{2.41}$$

This is the rate at which single-photons are converted into single-phonons, or in other words the rate at which energy is transduced from the optical mode to the mechanical mode [18].

We can now compute radiation pressure force from the interaction Hamiltonian. The general expression for the radiation pressure force is the derivative with respect to displacement of the interaction Hamiltonian $\hat{F} = -d\hat{H}_{\text{int}}/d\hat{x}$ [2]. For our system we obtain:

$$\hat{F} = \hbar \frac{g_0}{x_{\text{zpf}}} \hat{a}^\dagger \hat{a} = \hbar G \hat{a}^\dagger \hat{a}. \tag{2.42}$$

If we replace $G = \omega_{\text{c}}/L$ and $\bar{n}_{\text{c}} = \hat{a}^\dagger \hat{a}$ we arrive at the same expression for the radiation pressure force for the Fabry-Perot cavity as shown in Eq. 2.38, as expected.

2.3.3 Rotating Wave Approximation

A standard technique to simplify the analysis of our system easier is to perform the rotating wave approximation. Applying the unitary transformation $\hat{U} = e^{i\omega_{\text{l}}\hat{a}^\dagger\hat{a}}$ effectively switches our frame of reference to one that rotates with the laser frequency ω_{l} [2]. In other words, frequencies that are far from ω_{l} average to zero and can be ignored. In addition to this, it also makes the driving terms time independent [2]:

$$\hat{U}\left(\hat{a}^\dagger e^{-i\omega_{\text{l}}t} + \hat{a}e^{i\omega_{\text{l}}t}\right)\hat{U}^\dagger = \hat{a}^\dagger + \hat{a}. \tag{2.43}$$

Performing the unity transformation $\hat{H}_{\text{new}} = \hat{U}\hat{H}_{\text{old}}\hat{U}^\dagger - i\hbar\hat{U}\partial\hat{U}^\dagger/\partial t$ yields [2]:

$$\hat{H} = -\hbar\Delta\hat{a}^\dagger\hat{a} + \hbar\omega_{\text{m}}\hat{b}^\dagger\hat{b} - \hbar g_0\hat{a}^\dagger\hat{a}(\hat{b} + \hat{b}^\dagger) + ... \tag{2.44}$$

Where we have defined a new parameter called the detuning $\Delta = \omega_{\text{l}} - \omega_{\text{c}}$. Contained in the (...) are terms such as the driving and decay terms, which we omit from this Hamiltonian since they are much better described using input-output theory.

2.3.4 Linearizing the Hamiltonian

The mechanical mode of our system slightly distorts the geometry of our optomechanical crystal (OMC), which leads to a modulation of the optical

mode [2]. This allows us to approximate this modulation of the optical mode as an average coherent mode $\bar{\alpha}$ plus a fluctuating term $\delta\hat{a}$ [2]:

$$\hat{a} = \bar{\alpha} + \delta\hat{a}, \tag{2.45}$$

which can then be inserted into our interaction Hamiltonian and expanded in orders of $\bar{\alpha}$. This expansion gives [2]:

$$\hat{H}_{\text{int}} = -\hbar g_0(|\bar{\alpha}|^2 + \bar{\alpha}^*\delta\hat{a} + \bar{\alpha}\delta\hat{a}^\dagger + \delta\hat{a}^\dagger\delta\hat{a})(\hat{b} + \hat{b}^\dagger), \tag{2.46}$$

but can be simplified by assuming that $\bar{\alpha} = \bar{\alpha}^* = \sqrt{\bar{n}_\text{c}}$ is real valued. The $|\bar{\alpha}|^2$ term then just represents an average radiation pressure force $\bar{F} = \hbar G|\bar{\alpha}|^2$, and can be omitted by moving the displacement's origin by $\delta\bar{x} = \bar{F}/m_{\text{eff}}\omega_\text{m}^2$ and by shifting the detuning to $\Delta_{\text{new}} = \Delta_{\text{old}} + G\delta\bar{x}$ [2]. We can also omit the $\delta\hat{a}^\dagger\delta\hat{a}$ term since it is significantly smaller than $\bar{\alpha}$. Expanding out the rest of the terms leads to the full Hamiltonian given by [2]:

$$\hat{H} = -\hbar\Delta\hat{a}^\dagger\hat{a} + \hbar\omega_\text{m}\hat{b}^\dagger\hat{b} - \hbar g_0\sqrt{\bar{n}_\text{c}}(\delta\hat{a}^\dagger\hat{b} + \delta\hat{a}^\dagger\hat{b}^\dagger + \delta\hat{a}\hat{b} + \delta\hat{a}\hat{b}^\dagger), \tag{2.47}$$

and allows for defining the cavity enhanced optomechanical coupling strength [2], $g \equiv g_0\sqrt{\bar{n}_\text{c}}$. This is named cavity enhanced because of its dependence on the term $\sqrt{\bar{n}_\text{c}}$ meaning that we can tune the coupling strength by adjusting the number of photons inside our cavity.

2.3.5 Coupled Optomechanical Equations of Motion

The interaction term we added to our Hamiltonian will also result in additional terms that must be included in the input-output equations of motion. Similar to our derivation of the uncoupled equations of motion, we can use Heisenberg's equation to derive the coupled equations of motion [2]. Performing this derivation results in the interaction terms:

$$\dot{\hat{a}}_{\text{int}} = ig_0(\hat{b} + \hat{b}^\dagger)\hat{a}, \tag{2.48}$$

$$\dot{\hat{b}}_{\text{int}} = ig_0\hat{a}^\dagger\hat{a}, \tag{2.49}$$

being added. The resulting equations of motion are given by [2]:

$$\dot{\hat{a}}(t) = i\Delta\hat{a}(t) - \frac{\kappa}{2}\hat{a}(t) + ig_0(\hat{b} + \hat{b}^\dagger)\hat{a} + \sqrt{\kappa_{\mathrm{e}}}\hat{a}_{\mathrm{in}}, \tag{2.50}$$

$$\dot{\hat{b}}(t) = -i\omega_{\mathrm{m}}\hat{b}(t) - \frac{\Gamma_{\mathrm{m}}}{2}\hat{b}(t) + ig_0\hat{a}^\dagger\hat{a} + \sqrt{\Gamma_{\mathrm{m}}}\hat{b}_{\mathrm{in}}(t). \tag{2.51}$$

From these two equations of motion we can see that the optical mode will be shifted by the mechanics due to its motion about its center of mass $\hat{x} = x_{\mathrm{zpf}}(\hat{b} + \hat{b}^\dagger)$, while the mechanical mode will be shifted based on the number of photons in the cavity $\hat{a}^\dagger\hat{a}$.

Chapter 3

Photonic crystal design, simulation, and fabrication

The first OMCs were designed and fabricated by the Oskar Painter lab at Caltech in 2009 [3]. The original device was made by periodically patterning rectangular shaped holes into an optical waveguide in such a way that it supported both optical and mechanical modes. Future iterations optimized the unit cell geometry, using circles and ellipses instead of rectangles [21]. Inspired by the success of these devices, and since previous members of the group have used elliptical hole unit cells in the past [16], we decided to base our designs off of the elliptical hole unit cell geometry.

An essential consideration in the design of an OMC is what material to use. Materials commonly used in the fabrication of OMCs include: silicon [3], silicon nitride [22, 23], gallium arsenide [16, 24, 25], aluminum nitride [26–28], gallium phosphide [29, 30], diamond [31–33], and lithium niobate [34, 35]. To date it is not yet certain which material will produce the best devices, so material choice is largely dependent on personal preference and tool and material availability. For the work presented here we chose to use stoichiometric silicion nitride (SiN). This choice was motivated by the high intrinsic tensile stress of SiN, which leads to higher mechanical resonance frequencies, as well as SiN's large optical bandgap, reducing optical heating [36, 37]. Another motivating factor was that SiN has been used in optomechanical systems successfully in the past. SiN trampoline resonators with quality factors ($Q = \omega_c/\kappa$) greater than 10^7 at room temperature have been achieved [38, 39], while our group

has fabricated SiN nanostrings with quality factors of 10^6 at cryogenic temperatures [40].

This chapter will proceed as follows. Section 3.1 will discuss the crystal theory needed to find the plane wave solutions and dispersion relation for the optical and mechanical modes of the OMC, and then use index guiding and discrete translational symmetry to show that our solutions take the form of Bloch states. Section 3.2 will go over how we performed both unit cell and full device simulations for the OMC as well as construct band diagrams for the optical and mechanical modes of these devices. Lastly, in section 3.3 we describe the process flow we followed to fabricate these OMCs.

3.1 Crystal Theory

3.1.1 Optical Plane Waves

An OMC shares many similarities to periodic dielectric structures such as a Bragg mirror. In both cases we are concerned with how light in the form of electromagnetic waves behaves inside the medium. Following the derivations in references [19] and [41], we begin with Maxwell's equations for single mode electric $\mathbf{E}(\mathbf{x},t) = \mathbf{E}(\mathbf{x})e^{i\omega t}$ and magnetic $\mathbf{B}(\mathbf{x},t) = \mathbf{B}(\mathbf{x})e^{i\omega t}$ fields [41]:

$$\nabla \cdot \epsilon(\mathbf{x})\mathbf{E} = 0, \tag{3.1}$$

$$\nabla \cdot \mathbf{B} = 0, \tag{3.2}$$

$$\nabla \times \mathbf{E} = -i\omega\mathbf{B}(\mathbf{x}), \tag{3.3}$$

$$\nabla \times \mathbf{B} = i\frac{\omega\epsilon_r(\mathbf{x})}{c^2}\mathbf{E}(\mathbf{x}). \tag{3.4}$$

Here $\epsilon(\mathbf{x}) = \epsilon_0\epsilon_r(\mathbf{x})$ where ϵ_0 is the permittivity of free space, $\epsilon_r(\mathbf{x})$ is the relative permittivity at position $\mathbf{x}$, and we have used the relation $c = 1/\sqrt{\mu_0\epsilon_0}$. We can derive the eigenvalue equation for our system by inserting Eq. 3.3 into Eq. 3.4, yielding:

$$\nabla \times \frac{1}{\epsilon_r(\mathbf{x})}\nabla \times \mathbf{B}(\mathbf{x}) = \frac{\omega^2}{c^2}\mathbf{B}(\mathbf{x}), \tag{3.5}$$

where we have defined the Hermitian operator $\hat{\Theta}$ [19]:

$$\hat{\Theta}\mathbf{B}(\mathbf{x}) = \nabla \times \frac{1}{\epsilon_r(\mathbf{x})}\nabla \times \mathbf{B}(\mathbf{x}). \tag{3.6}$$

One possible set of solutions to this eigenvalue problem are the plane wave solutions $\mathbf{B}(\mathbf{x}) = \mathbf{B}_0 e^{(i\mathbf{k}\cdot\mathbf{x})}$ with eigenvalues $|\mathbf{k}|^2/\epsilon_r$ and dispersion relation $(\omega/c)^2 = |\mathbf{k}|^2/\epsilon_r$.

Index Guiding

Consider a waveguide with index n_1 suspended in air with index n_2. When light is incident on the interface between the waveguide and air two quantities must be conserved: frequency and the component of the wave vector parallel to the interface [41]. The parallel component of the wave vector is given by:

$$k_\parallel = |\mathbf{k}| \sin\theta = \frac{n\omega}{c} \sin\theta, \tag{3.7}$$

from which we obtain Snell's law by requiring the parallel component on both sides of the interface be equal to each other:

$$k_{1,\parallel} = \frac{n_1\omega}{c} \sin\theta_1 = \frac{n_2\omega}{c} \sin\theta_2 = k_{2,\parallel}, \tag{3.8}$$

$$n_1 \sin\theta_1 = n_2 \sin\theta_2. \tag{3.9}$$

No such relationship exists for the perpendicular component of the wave vector, which leads to a concept called index guiding [41]. To explain this, consider modes that are not confined by the waveguide. Far from the waveguide our modes are free-space plane waves:

$$\omega = c|\mathbf{k}| = c\sqrt{k_\parallel^2 + k_\perp}, \tag{3.10}$$

where $k_\perp$ can take any real value. For a given value of $k_\parallel$ we will have infinitely many possible frequencies above $ck_\parallel$. In a band diagram this region of modes is called the light cone, and the lower limit $\omega = ck_\parallel$ is called the light line [19, 41].

Below the light line the only solutions that exist will have imaginary $k_\perp$ given by:

$$k_\perp = \pm i\sqrt{k_\parallel^2 - \omega^2/c^2}, \tag{3.11}$$

representing modes that decay exponentially away from the waveguide [41]. These modes called index guided modes will be confined to the waveguide, and they will produce a discrete spectrum of frequencies that depend on $k_\parallel$. Fig. 3.1B) provides a simple example of the band diagram of a waveguide.

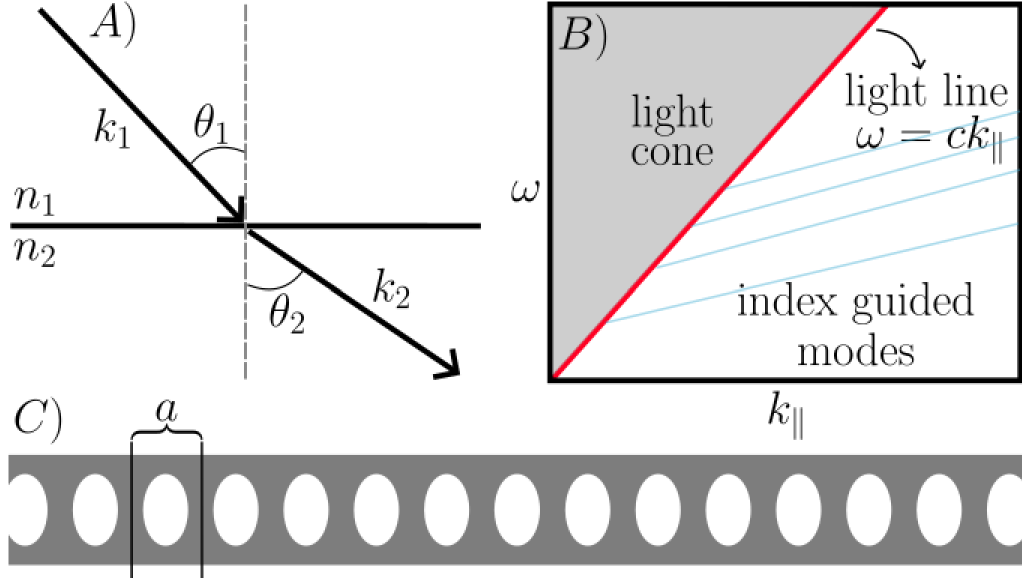

Figure 3.1: A) A schematic of how light rays refract at the interface of two materials with index n_1 and n_2. The parallel component of the wavevectors of the two light rays must be conserved, from which one can derive Snell's law. B) An example of a band diagram for a waveguide. The light line ($\omega = ck_\parallel$) is shown in red. Above this line there is a continuous spectrum of modes called the light cone, and below this line there is discrete spectrum of modes called index guided modes. C) Example of a waveguide periodically patterned with holes which will exhibit discrete translational symmetry. Each hole is separated by a distance a, such that the system is unchanged when moving up or down the waveguide in steps of na where $n \in \mathbb{Z}$.

Discrete Translational Symmetry

Now consider a waveguide periodically patterned with holes separated by a unit cell width a such as the one shown in Fig. 3.1C). This system exhibits discrete translational symmetry [41], meaning that our system is unchanged if we move up or down the waveguide in steps of size na where $n \in \mathbb{Z}$. For each n, we define the translation operator:

$$T_n f(z) \equiv f(z + na), \tag{3.12}$$

which shifts the z coordinate of our solution by na. This translation operator can be used to classify our solutions, but in order to do so it must satisfy two conditions: Our permittivity must be translationally periodic $\hat{T}_n \epsilon(z) = \epsilon(z + na) = \epsilon(z)$ and we must also have $[\hat{T}_n, \hat{\Theta}] = 0$ [41]. The first condition is known to hold based on the geometry of our system. Following the derivation in reference [41], the second condition can be shown to be true by showing

how the commutator acts on the state $\mathbf{B}(\mathbf{x})$:

$$[\hat{T}_n, \hat{\Theta}]\mathbf{B}(\mathbf{x}) = \hat{T}_n \left(\nabla \times \frac{1}{\epsilon_r(\mathbf{x})} \nabla \times \mathbf{B}(\mathbf{x}) \right) - \left(\nabla \times \frac{1}{\epsilon_r(\mathbf{x})} \nabla \times \hat{T}_n \mathbf{B}(\mathbf{x}) \right), \tag{3.13}$$

$$= \hat{T}_n \left(\frac{\omega^2}{c^2} \mathbf{B}(\mathbf{x}) \right) - \left(\frac{\omega^2}{c^2} \hat{T}_n \mathbf{B}(\mathbf{x}) \right) = 0. \tag{3.14}$$

Satisfying these two conditions means that we can write the new eigenvalue equation $\hat{T}_n \mathbf{B}(\mathbf{x}) = \alpha \mathbf{B}(\mathbf{x})$. This new eigenvalue equation has a simple set of eigenvalue functions with the form e^{ikz} and eigenvalues e^{ikna}. By inspection we can see that the functions e^{ikz} and $e^{i(k+2\pi m/a)z}$ are degenerate for $m \in \mathbb{Z}$, therefore, after defining the primitive reciprocal lattice vectors $b = (2\pi/a)\hat{z}$, we must have:

$$\mathbf{B}(\mathbf{x}) = \sum_m c_m(x, y) e^{i(k+mb)z}, \tag{3.15}$$

$$= e^{ikz} \sum_m c_m(x, y) e^{imbz}, \tag{3.16}$$

$$= \mathbf{u}(x, y, z) e^{ikz}, \tag{3.17}$$

where the c_m terms are expansion coefficients and $\mathbf{u}(x, y, z)$ is periodic in z such that $\mathbf{u}(x, y, z + na) = \mathbf{u}(x, y, z)$ [41].

The result of discrete translational symmetry are solutions that are the product of plane waves and a periodic function. Solutions of this form are called Bloch states and have the special property that states that differ by integer multiples of the reciprocal lattice vector are identical [41]. This means that we can significantly reduce the range of wave vectors we look at to the range $-\pi/a \leq k < \pi/a$ called the first Brillouin zone. Our system can be further reduced to the range $0 \leq k < \pi/a$ called the irreducible Brillouin zone due to the time-reversal symmetry of our system [19].

3.1.2 Mechanical Plane Waves

Following the derivation shown in reference [19], a similar set of solutions can be found for the displacement field $u(\mathbf{r}, t)$ of acoustic waves propagating in a solid. For a homogeneous, linear elastic medium with no body forces, the

equation of motion is given by [19]:

$$\frac{1}{\rho(\mathbf{r})}\nabla_j C_{ijmn}(\mathbf{r})\nabla_n u_m(\mathbf{r},t) = \frac{\partial^2}{\partial t^2}u_i(\mathbf{r},t), \tag{3.18}$$

where $\rho(\mathbf{r})$ is the mass density and C_{ijmn} is the rank 4 elasticity tensor. This tensor is often symmetric such that $C_{ijmn} = C_{jimn} = C_{ijnm} = C_{jinm}$, which allows us reduce the $3 \times 3 \times 3 \times 3$ tensor to a 6×6 matrix using the mapping [19]:

$$\begin{aligned} xx &\rightarrow 1, \\ yy &\rightarrow 2, \\ zz &\rightarrow 3, \\ yz, zy &\rightarrow 4, \\ xxz, zx &\rightarrow 5, \\ xy, yx &\rightarrow 6. \end{aligned} \tag{3.19}$$

This dimension reduction is called Voigt notation [42], and the elasticity tensor for an isotropic medium using this notation is given by:

$$C(\mathbf{r}) = \begin{bmatrix} c_{11} & c_{12} & c_{12} & 0 & 0 & 0 \\ c_{12} & c_{11} & c_{12} & 0 & 0 & 0 \\ c_{12} & c_{12} & c_{11} & 0 & 0 & 0 \\ 0 & 0 & 0 & c_{44} & 0 & 0 \\ 0 & 0 & 0 & 0 & c_{44} & 0 \\ 0 & 0 & 0 & 0 & 0 & c_{44} \end{bmatrix}, \tag{3.20}$$

where $c_{11} = K(\mathbf{r}) + \frac{4}{3}\mu(\mathbf{r})$, $c_{12} = K(\mathbf{r}) - \frac{2}{3}\mu(\mathbf{r})$, and $c_{44} = \mu(\mathbf{r})$, where $K(\mathbf{r})$ is the bulk modulus and $\mu(\mathbf{r})$ is the shear modulus.

Due to the discrete translational symmetry of the waveguide, the displacement takes the form of a Bloch state:

$$u_i(\mathbf{r},t) = e^{i\mathbf{k}\cdot\mathbf{r}}u_i(\mathbf{r})e^{i\omega_m t}. \tag{3.21}$$

Inserting this into Eq. 3.18 results in the eigenvalue equation:

$$\hat{\Theta}u_i(\mathbf{r},t) = \frac{\omega_m^2}{c_t^2}u_i(\mathbf{r},t), \tag{3.22}$$

where:

$$\hat{\Theta}u_i(\mathbf{r},t) = \frac{1}{\rho(\mathbf{r})}\nabla_j C_{ijmn}(\mathbf{r})\nabla_n u_m(\mathbf{r},t), \tag{3.23}$$

is a Hermitian operator similar to what we had obtained for the optical case. This eigenequation has eigenvalues $|\mathbf{k}|^2 = (k_x^2 + k_y^2 + k_z^2)$ and the dispersion relation $|\mathbf{k}|^2 = \omega_m^2/c_t^2$ where c_t is the transverse sound velocity of the acoustic waves within the material [43]. These solutions can then be plotted in the first Brillouin zone to visualize the band structure of these mechanical modes.

3.2 Simulations

Designing and simulating the OMC was done primarily through the use of COMSOL Multiphysics [44] in conjunction with MATLAB [45]. COMSOL was used to build the simulation geometry and run the numerical simulations, while MATLAB was connected with COMSOL using Simulink in order to control parameter sweeps and data collection. Initial COMSOL simulations were performed to determine a good unit cell geometry for the mirror unit cell of the OMC. The results of these simulations were used to generate optical and mechanical band diagrams of the OMC. Afterwards, simulations of the full OMC were performed to calculate values such as the quality factor and optomechanical coupling rate. The goal when designing the OMC is to find a geometry with large optical and mechanical quality factors such that we are sideband resolved, have good optomechanical coupling, and a high mechanical frequency.

3.2.1 Unit Cell Simulations

As shown in Fig. 3.2A), our unit cell can be characterized by its width, ellipse semi axes hz and hx, thickness (not shown), and the unit cell width a. The goal of simulating the unit cell of our OMC is to generate k vs ω plots in the first Brillouin zone. These plots are called band diagrams and they provide a visual representation of the different optical and mechanical modes of our unit cell.

When performing the optical simulations, some of the field will exist outside the waveguide and must also be simulated. Fig. 3.2B) shows that this can be done by surrounding the unitcell with a box of air and capping this

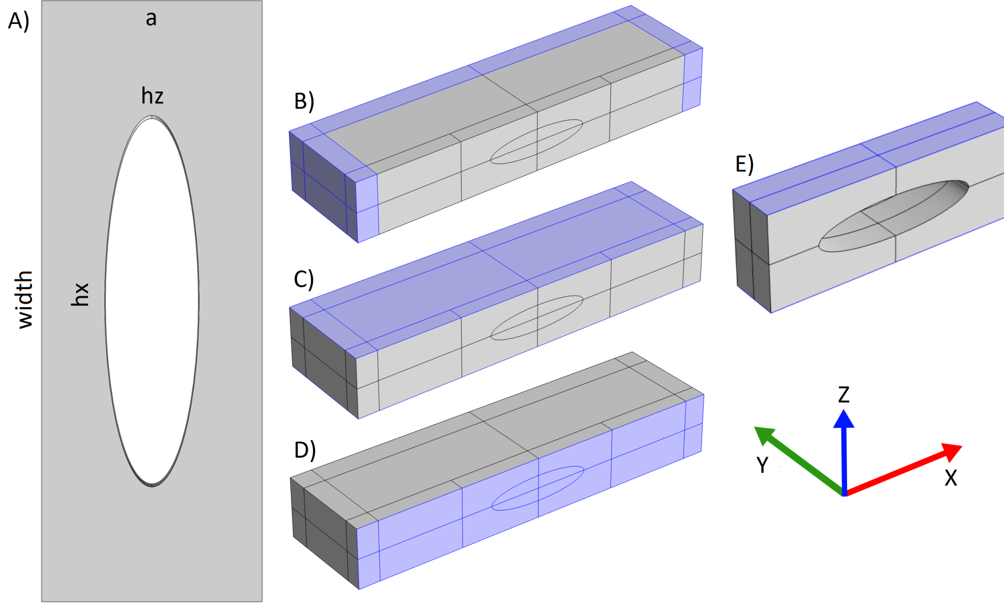

Figure 3.2: Examples of the unit cell geometry used in our COMSOL simulations. A) Unit cell geometry with labels for the unit cell width (a), the ellipse semi-axes (hx and hy), and the width of the waveguide. The unitcell also has a thickness t, but this is not shown in this figure. Figures B-D show the geometry of the unit cell and air box used for the optical simulation. The blue shaded regions are B) the PML layer, C) the periodic boundary condition, and D) the perfect magnetic conductor boundary condition. E) Geometry of the unit cell for the mechanics simulation with the periodic boundary condition labeled in blue. Note that the periodic boundary conditions are placed on both the shown surface and the surface opposite the one shown.

box with perfectly matched layers (PMLs). PMLs are open boundaries that imitate a non-reflecting infinite domain [44]. These prevent fields that leak outside the waveguide from reflecting off the boundary and leaking back into the waveguide. Note that this air box is not needed for the mechanics simulation.

In order to simulate a periodically repeating unit cell we add a Floquet periodic condition [44] on both sides of the unit cell. Fig. 3.2C) and E) show how this was done for optics and mechanics respectively. This condition allows us to define a Floquet vector $\vec{k_F} = \{k_x, k_y, k_z\}$ that determines the periodicity of our unit cell. Our unit cell is only periodic in z so we set $k_x = k_y = 0$ and $k_z = 2\pi k/a$ where $k = [0, 0.5]$ is a unitless factor that is used in generating band diagrams. The optical simulation has one more additional boundary

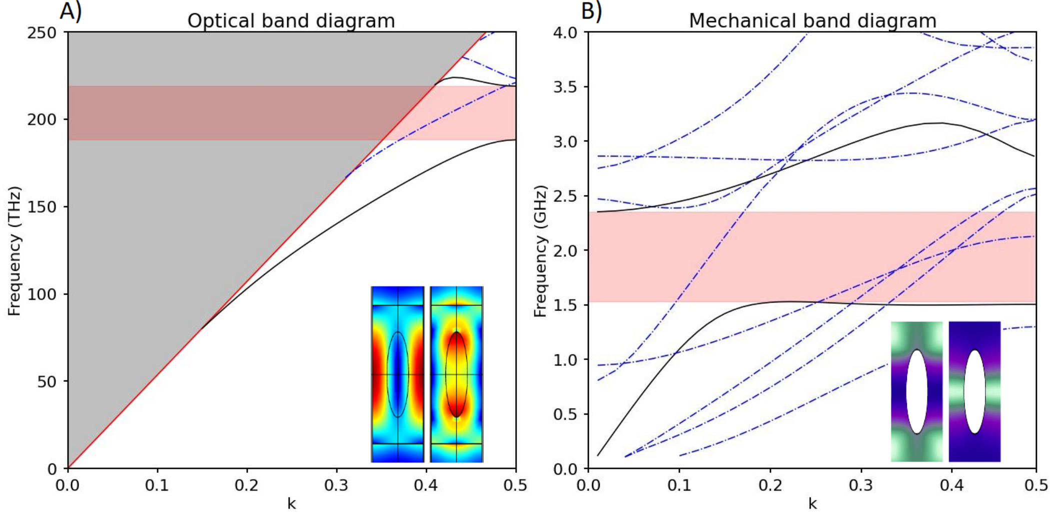

Figure 3.3: A) Optical band diagram for our unit cell geometry. The grey region represents the continuum of modes that exist outside the unit cell, while the white region represents index guided modes of the unit cell. The light line $\omega = ck$ separates these two regions. The black lines and blue dot-dashed lines represent modes with different polarizations (see text). The red shaded region is the quasi-bandgap between the lower and upper black bands. The inset shows the simulated electric field profiles for the lower and upper bands labeled with a black line. B) Mechanical band diagram for our unit cell geometry. The black lines and blue dot-dashed lines represent symmetric and non-symmetric modes respectively. Simulated displacement field profiles are shown in the inset for the lower and upper bands respectively.

condition that greatly reduces computation time. Fig. 3.2D) shows how we place a perfect magnetic conductor boundary that splits our unit cell in half along its thickness. This imposes symmetry for the electric fields in the unit cell, allowing us to simulate only half of our geometry.

We can simulate all the modes needed to generate the band diagrams by performing a parameter sweep of k from 0 to 0.5, which translates to sweeping k_z from 0 to π/a. As predicted in section 3.1, our optical band diagram (Fig. 3.3A)) has both a continuous mode region and a discrete mode region separated by the light line $\omega = ck$. Modes within the discrete mode region depend on polarization [19]. The black lines represent modes polarized along the xz-plane, while the blue dot-dashed modes are modes polarized along the yz-plane. As shown in red, by adjusting the polarization of light entering into our system we can filter out the yz-polarized modes, generating a quasi-bandgap in the range $\omega_c = (188.2, 218.9)$ THz. Fig. 3.3B) shows the mechanical band

diagram for our unit cell. Here the two modes labeled by a black line are modes that are symmetric about the yz-plane, while all other modes are labeled by a blue dot-dashed line. Once again we see a quasi-bandgap which spans from $\omega_m = 1.50$ GHz to $\omega_m = 2.47$ GHz. The insets of each figure show the electrical field or the displacement field profiles of the two bands respectively.

3.2.2 Full Device Simulations

The goal of simulating the full OMC is to now apply a modification to the unit cell geometry such that we can simultaneously localize an optical mode and a mechanical breathing mode to the center of the OMC. In Fig. 3.4A) we show how we can split the OMC into two categories of unit cells: two sections of mirror unit cells and a defect unit cell in between. The defect unit cell is made by adjusting the size of the holes (hx and hz) and the unit cell width a of the mirror unit cell such that frequencies that used to fall within the band gap now lie within one of the bands. In order to prevent scattering, there must be a smooth transition between the mirror unit cell and the defect unit cell. Taking inspiration from reference [19], our transition occurred over 7 unit cells and changes in a, hx, and hz had the form:

$$a = a_{\text{mirror}} - \delta a \left(2\,(j)^3 - 3\,(j)^2 + 1\right), \tag{3.24}$$

$$hx = hx_{\text{mirror}} - \delta hx \left(2\,(j)^3 - 3\,(j)^2 + 1\right), \tag{3.25}$$

$$hz = hz_{\text{mirror}} - \delta hz \left(2\,(j)^3 - 3\,(j)^2 + 1\right), \tag{3.26}$$

where $j = n/7$ for $n \in [0, 7]$ labels each transition unit cell. Variables a_{mirror}, hx_{mirror}, and hz_{mirror} represent mirror unit cell width and semi-axes respectively, while δa, δhx, and δhz, are the changes between the mirror and defect unit cell for these same variables. We can provide further control of the slope of the transition by remapping the values of j to:

$$m = \begin{cases} \frac{1}{2}\,(2j)^{\epsilon} & j < 0.5, \\ 1 - \frac{1}{2}(2(1-j))^{\epsilon} & j \geq 0.5, \end{cases} \tag{3.27}$$

where ϵ can be adjusted to fine tune the slope of the transition [19].

As shown in Fig. 3.4A), after the transition region we repeat the mirror unit cell 12 times. This was found to be the optimal number of unit cells needed to

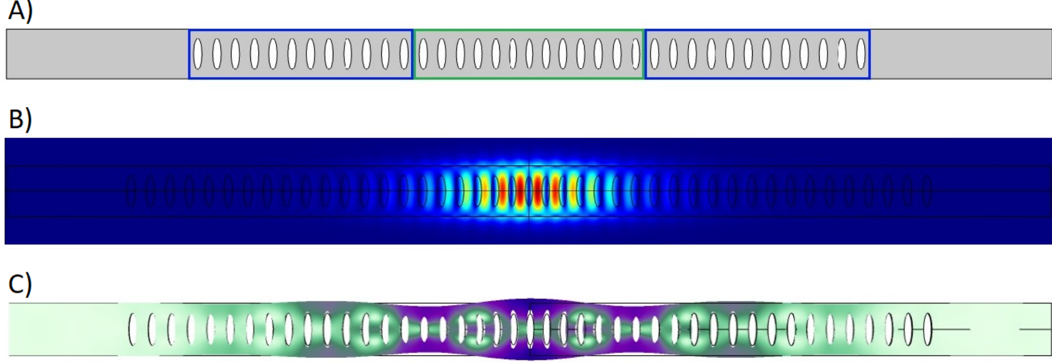

Figure 3.4: A) Schematic of our OMC with the mirror regions outlined in blue and the defect region outlined in green. B) Simulated optical mode electric field profile. Notice how the field is confined to the defect region. C) Simulated mechanical mode displacement field profile. Comparing the optical and mechanical modes notice that there is a large amount of spatial overlap between the two modes.

create a high-reflectivity mirror section that confined our optical mode to the defect region. Using more mirror unit cells than 12 had diminishing returns. Fig. 3.4B) and Fig. 3.4C) show the field profile of the simulated optical and mechanical modes of the full OMC. The optical mode was found to occur at 202.26 THz while the mechanical mode occurred at 2.46 GHz, both of which exist within the bandgaps we predicted from the unit cell simulations.

Once the simulations are working, we can then perform calculations within COMSOL to predict many optomechanical characteristics of our OMC. From the optical simulation, we can calculate the optical mode volume using [18, 46]:

$$V_{\text{opt}} = \frac{\int \epsilon(\mathbf{r})|\mathbf{E}(\mathbf{r})|^2 dV}{\max(\epsilon(\mathbf{r})|\mathbf{E}(\mathbf{r})|^2)}, \tag{3.28}$$

where $\epsilon(\mathbf{r})$ is the relative permittivity and $|\mathbf{E}(\mathbf{r})|$ is the normalized electric field calculated numerically. Similarly, we can also calculate the mechanical mode volume using [18, 46]:

$$V_{\text{m}} = \int \frac{|Q(\mathbf{r})|}{\max(|Q(\mathbf{r})|)^2} dV, \tag{3.29}$$

where $Q(\mathbf{r})$ is the numerically calculated displacement field. From these calculations, COMSOL predicted that $V_{\text{opt}} = 0.364$ μm^3 and $V_{\text{m}} = 1.39$ μm^3. The effective mass can then be calculated from the mechanical mode volume by multiplying by the density, giving a value of $m_{\text{eff}} = 4.33$ pg, which can then

be inserted into our expression for $x_{\rm zpf}$ yielding $x_{\rm zpf} = 0.886$ fm. Lastly, the optomechanical coupling rate g can be estimated by computing the overlap integral of the optical and mechanical modes. This method of calculating g gives the moving boundary optomechanical coupling rate [18, 46]:

$$g_{\rm mb} = \frac{\omega_c x_{\rm zpf}}{2V_{opt}} \int \mathbf{u}(\mathbf{r}) \cdot \mathbf{n}(\mathbf{r}) \left[(\epsilon_2 - \epsilon_1)|\mathbf{E}_{\parallel}(\mathbf{r})|^2 - \frac{\epsilon^2(\mathbf{r})|\mathbf{E}_{\perp}(\mathbf{r})|^2}{\epsilon_2 - \epsilon_1} \right] d\mathbf{A}, \quad (3.30)$$

which is maximized for small optical mode volumes and large $x_{\rm zpf}$ paired with a large overlap integral. These simulations predicted that the moving boundary optomechanical coupling rate of these devices would be $g_{\rm mb}/2\pi = 348$ Hz.

3.3 Fabrication

The devices described in the previous two sections were fabricated at the University of Alberta in the NanoFAB Fabrication and Characterization Center [47]. The wafers were purchased from Rogue Valley Microdevices [37] and consist of a 300 nm layer of PECVD low-stress silicon nitride (SiN) deposited on silicon (Si). The fabrication process flow can be split into 4 parts: substrate cleaning and preparation, electron beam lithography (EBL), reactive ion etching (RIE), and wet etching.

3.3.1 Substrate Cleaning and Preparation

The first step of fabrication is to dice the wafer into smaller, easier to work with chips. We chose to dice the wafer into 10 mm x 10 mm chips with 5 mm x 5 mm score lines on the back using the disco DAD 3240 dicing saw available at the NanoFAB. This allows us to fabricate 4 devices at once, and then break the chip along the score lines after fabrication. Next, the chips are cleaned by soaking them in a piranha solution, made by adding 1 part hydrogen peroxide to 3 parts sulfuric acid, for 20 minutes.

Once the chips are diced and cleaned, we deposit a 50 nm film of aluminum (Al) onto the chips using the KJLC CMS-18 sputtering system (nicknamed “Floyd” at the nanofab). Al is conductive, so during EBL the Al will help dissipate extra charge, providing better pattern resolution. The primary reason for depositing this layer of Al is that after EBL the Al layer will serve

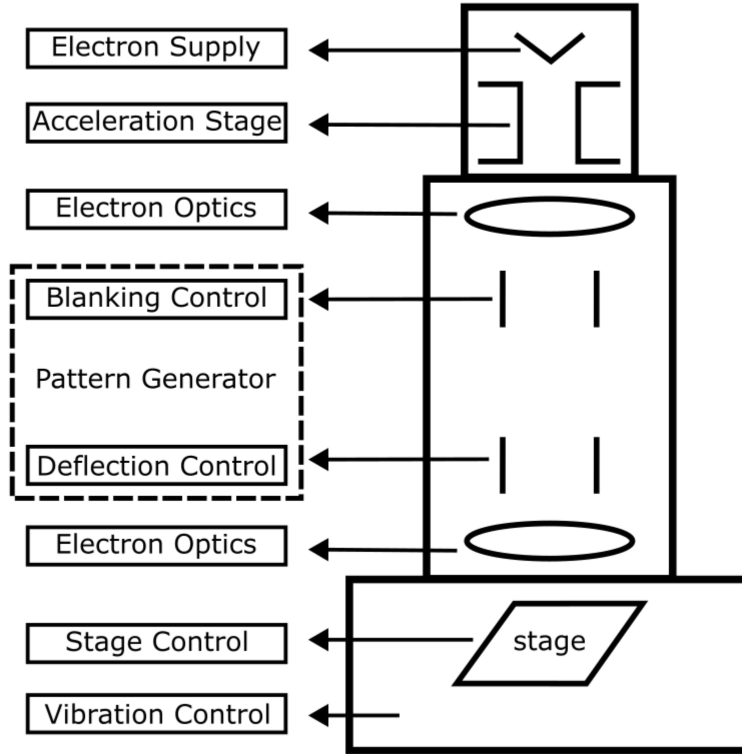

Figure 3.5: Schematic of how an EBL system works. Taken from [5].

as a hard mask material for etching the SiN layer. The last step of substrate preparation is to spin on a layer of electron beam resist. The electron beam resist we used is ZEP 520A, which was spun onto our chips at 3000 rpm for 60 seconds and then baked at 180°C for 5 minutes on a hot plate.

3.3.2 Electron Beam Lithography

EBL is one of the most important and powerful techniques for creating nanometer scale devices [5]. EBL works similar to film photography. The films used for photography are coated in a light sensitive material such that when a picture is taken (i.e. the film is exposed to light) the films undergo a slight chemical reaction. This chemical reaction does not alter the film visually, but we can bring out the colours of the photo by soaking the films in a developer solution. Instead of using light to expose the electron beam resist we spun on our chips, the EBL technique uses a focused beam of electrons. This allows for drawing nanometer scale patterns into the resist. A schematic of a typical

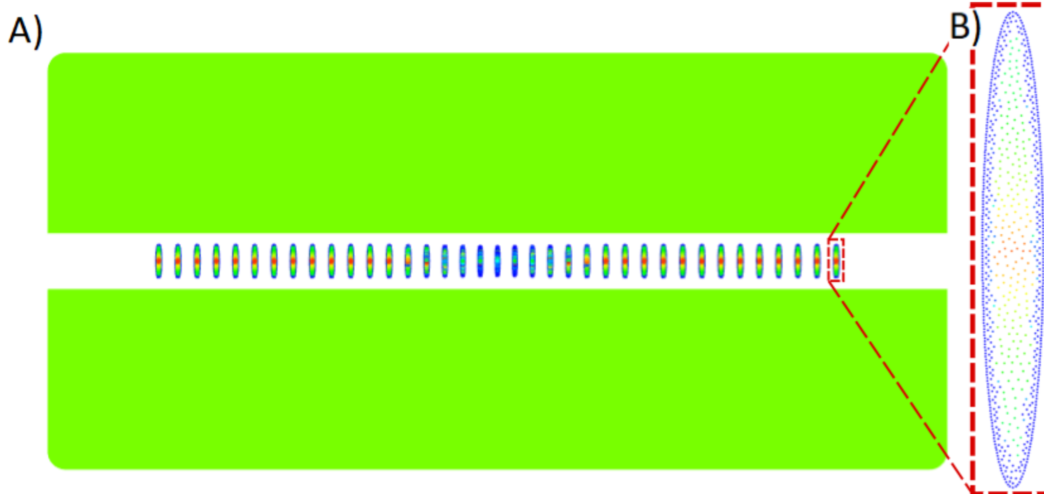

Figure 3.6: A) Full device geometry and B) hole geometry for the GDSII files used in this thesis. The bulk area around the waveguide drawn in green is patterned using straight or curved lines while the holes are patterned using a dot-dose array. The colour of the dots corresponds to the dose that dot receives, with red dots receiving a higher dose while blue dots receive a lower dose.

EBL system is shown in Fig. 3.5, while the EBL system that we used to create our OMCs was the Raith 150$^{\mathrm{TWO}}$ commercial EBL system. The Raith reads patterns with the GDSII filetype, so the first step in EBL is to take the design we made in COMSOL and write Python or Matlab code that draws it in the GDSII format.

Proximity effects due to scattering of electrons greatly complicates our pattern design. Scattering causes a broadening of the electron beam after it enters the electron beam resist due to low energy elastic collisions [5]. Under most circumstances this broadening is fairly predictable, and can be mitigated by using a higher energy electron beam and by making GDSII patterns slightly larger or smaller than predicted. Very small patterns such as the holes in our unit cells require much more precise control over how the electron beam resist is exposed. This is done through the use of a dot-dose array as shown in Fig. 3.6B). Each dot receives a specified dose of electrons, allowing for precise control over how the resist is exposed. The Matlab function responsible for creating the dot-dose array was originally written by the fabrication group manager at the nanofab, Aaron Hryciw [48], and then modified to fit my purpose.

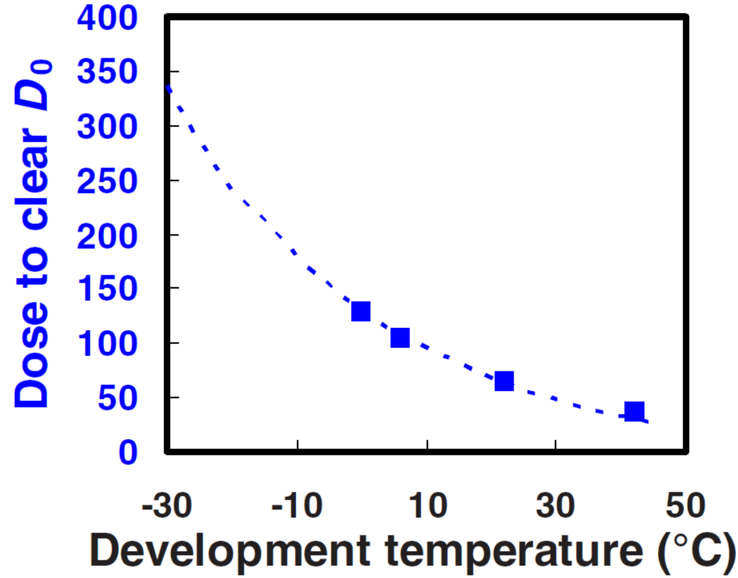

Figure 3.7: The above plot is taken from [49]. This plot compares the dose needed to fully develop the exposed electron beam resist (dose to clear) to the temperature of the developer used. When taking this data the authors submerged the chips in the developer for 10 s. The four square data points represent their four separate trials, while the blue dashed curve is a fit to their data points.

After exposure, the chips are dipped in the developer liquid ZED N50 which dissolves the sections of electron beam resist that were exposed to the electron beam. The amount of electron beam resist that is dissolved greatly depends on the temperature of the liquid and length of time the chip is submerged. Fig. 3.7 shows a plot taken from [49] that compares the dose needed to fully develop the exposed electron beam resist to the temperature of the developer for a development time of 10 seconds. They found that lower temperatures greatly reduced the edge roughness of the patterns, which motivated our decision to develop our chips for 11s at -20 °C. Following development in ZED N50, the chips were dipped in an isopropyl alcohol solution for 20s at -20 °C which removes any remaining ZED N50, therefore preventing any further development. The necessary electron dose was then optimized based on these development parameters.

Etch Step	Cleaning	Conditioning	Etching	SF_6 clean
Chamber Pressure (mTorr)	10	4	4	10
Chamber Temperature (°C) 50	50	50	50	50
Forward ICP power (W)	1000	1000	1000	2000
RF power (W)	0	65	65	100
O_2 flow (sccm)	50	0	0	0
Cl_2 flow (sccm)	0	10	10	0
BCl_3 flow (sccm)	0	10	10	0
HBr flow (sccm)	0	30	30	0
SF_6 flow (sccm)	0	0	0	50
He backing (Torr)	0	10	10	10
Process time (hour:min:sec)	00:10:00	00:02:00	00:00:40	00:15:00

Table 3.1: Al RIE recipe used in this thesis. This is the nanofabs standard recipe for etching Al [47]. Adjustments to the etching steps process time can be made depending on the thickness of the Al layer.

3.3.3 Reactive Ion Etching

Reactive Ion Etching (RIE) combines physical etching with reactive etching through the use of a plasma-based dry etching technique [6]. For etching the Al layer of our chips, the plasma is formed from a gas consisting of Cl_2, BCl_3, and HBr, while the SiN etch uses a gas of C_4F_8 and SF_6. Within a vacuum chamber, a glow discharge plasma is formed from the reaction gas through the process of electron-impact ionization. The plasma contains many different species, such as radicals, positive and negative ions, electrons, and neutrons. The bottom surface of the vacuum chamber is made from a capacitively coupled electrode that is driven at a high frequency (typically 13.56 MHz [6]). The electrons in the plasma will be more strongly attracted to the electrode than the ions, so after plasma ignition the electrode will acquire a negative charge. The negative charge of the electrode will attract the positive ions in the plasma, resulting in the chip and electrode being bombarded with energetic, positive ions. At the same time as this ion bombardment, the radicals inside the plasma will react with the surface of the chip, creating a thin, uniform layer of material. This thin layer of material acts as a passivation layer that protects the vertical surfaces of the chip, which helps with etching straight vertical sidewalls. After the reaction, the reaction products diffuse away from the etching surface into

Etch Step	Cleaning	Conditioning	Etching
Chamber Pressure (mTorr)	20	10	10
Chamber Temperature (°C)	15	15	15
Forward ICP power (W)	2000	1200	1200
RF power (W)	150	20	20
DC bias (V)	200	40	40
O_2 flow (sccm)	100	0	0
C_4F_8 flow (sccm)	0	14	14
SF_6 flow (sccm)	10	14	14
He backing (Torr)	0	10	10
Process time (hour:min:sec)	01:00:00	00:20:00	00:07:00

Table 3.2: SiN RIE recipe used in this thesis. This etch recipe was given to me by my colleague Elham Zohari [50]. Adjustments to the etching steps process time can be made depending on the thickness of the SiN layer.

the bulk of the plasma before being pumped out of the chamber.

The Al hard mask was etched using the Oxford Cobra ICPRIE with the etch parameters provided in Table 3.1. This is the nanofabs standard recipe for etching Al [47]. The etching steps process time can be adjusted depending on the thickness of the Al layer. The SiN layer of our chips was etched using the Oxford Estrelas ICPRIE (DRIE) using the etch parameters provided in Table 3.2. This etch recipe was given to me by my colleague Elham Zohari [50], and we can similarly adjust the etching steps process time in order to fully etch the SiN layer. Note that the flow rate of gases in the chamber is measured using the units of standard cubic centimeters per minute (sccm). For both recipes, the first step is to clean the chamber to ensure that anything that may have been deposited on the walls of the chamber by the previous user does not contaminate our chips. Following this, we perform a conditioning step without our chips in the chamber. This is the same recipe we will use to etch our devices, but we first run it without our chips in the chamber so that the surface chemistry of the chamber can reach its steady-state [51]. After conditioning the chamber we mount our chips in the chamber and etch the chips for 40 seconds for the Al etch and for 7 minutes for the SiN etch. An additional cleaning step is needed after performing the Al etch that uses SF_6 instead of O_2. This is to prevent coating the surfaces of the chamber with

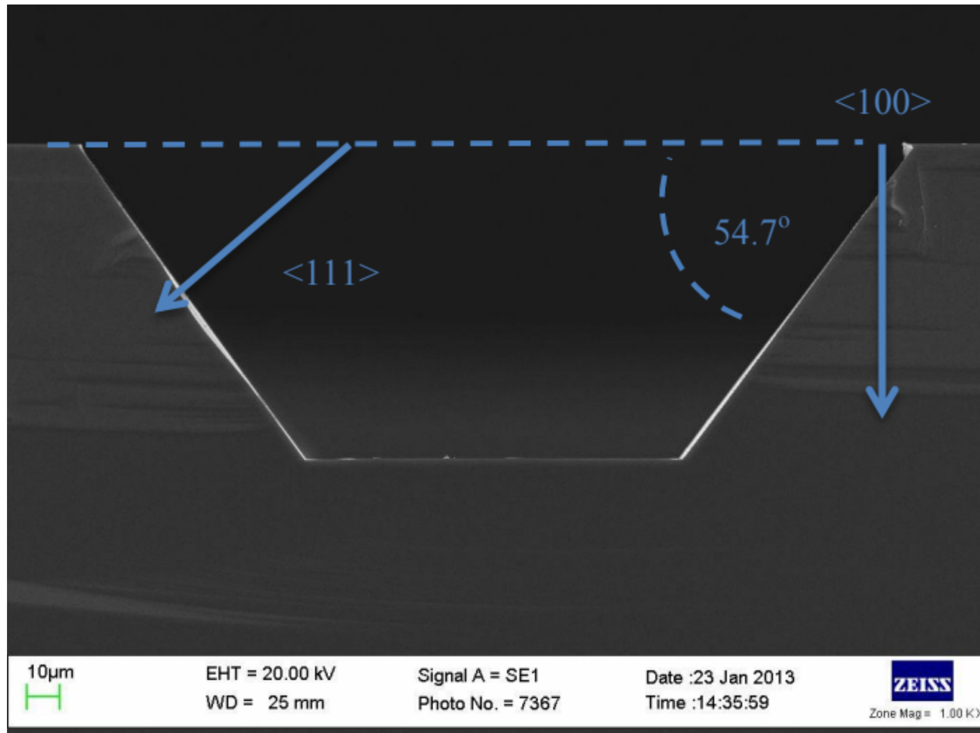

Figure 3.8: Example of how KOH etches Si along the $< 111 >$ crystal axis, leading to features with an angle of 54.7° when etching Si with a $< 100 >$ crystal orientation. Image taken from [53].

B_2O_3 which does not react with O_2 [52] and therefore can not be removed using a normal plasma clean.

3.3.4 Wet etching

Once the pattern is transferred to the SiN layer, the final step is to etch the Si underneath the SiN layer in order to suspend the OMC. It is very important to choose an etching technique that only targets the Si, so we decided to etch our devices using a 32% KOH solution which etches Si at a rate 7300 times faster than PECVD SiN [53]. KOH etching is anisotropic, with etching primarily happening along the $< 111 >$ crystal plane [53]. For Si with $< 100 >$ orientation used in this thesis, this means that the etch will proceed at an angle of 54.7° from the surface normal. This results in trenches or holes being shaped like triangular prisms, as shown in Fig. 3.8. The etch dimensions can

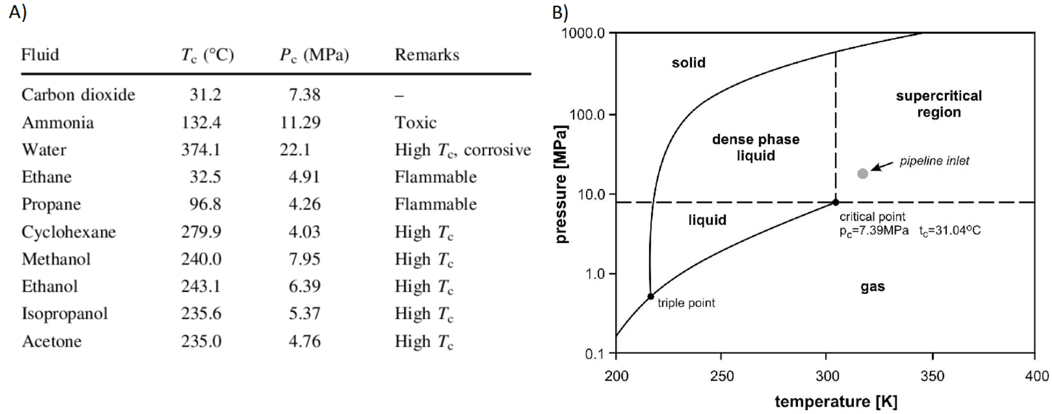

A)

Fluid	T_c (°C)	P_c (MPa)	Remarks
Carbon dioxide	31.2	7.38	–
Ammonia	132.4	11.29	Toxic
Water	374.1	22.1	High T_c, corrosive
Ethane	32.5	4.91	Flammable
Propane	96.8	4.26	Flammable
Cyclohexane	279.9	4.03	High T_c
Methanol	240.0	7.95	High T_c
Ethanol	243.1	6.39	High T_c
Isopropanol	235.6	5.37	High T_c
Acetone	235.0	4.76	High T_c

Figure 3.9: A) A collection of various liquids with their associated critical temperatures and pressures taken from [55]. B) Phase diagram for CO_2 taken from [54].

be calculated from the formula [53]:

$$A = B + 2 \times D \times \cot(54.7^\circ), \tag{3.31}$$

where A is the feature size in SiN, B is the feature size at the bottom, and D is the etch depth. To ensure that the OMCs were fully suspended, we etched our chips for one hour. Afterwards, we rinsed the chips in three deionized water baths before submerging them in an isopropyl alcohol (IPA) solution.

The last step in fabricating the OMCs is to dry the chips using a critical point dryer. If dried normally the surface tension of the liquid when transitioning from liquid to gas may be enough to damage the devices. Beyond the critical pressure and temperature there is no distinction between liquid and gas and no surface tension [54], making this an ideal method for drying fragile structures. As shown in Fig. 3.9A), many liquids have undesirable properties such as being flammable, toxic, or corrosive, so typically liquid CO_2 is used in critical point drying.

The Nanofab uses the Tousimis AutoSamdri 815B critical point dryer [56], which performs the critical drying process automatically. The user first fills the process chamber with enough IPA to cover their chip before transferring their chip to the chamber and sealing the chamber. The chamber is then cooled to 0°C and filled with liquid CO_2 while simultaneously purging the IPA from the chamber. At this point the chamber only contains liquid CO_2, so

when the chamber is heated to 38°C and pressurized to 9.3 MPa, the CO_2 becomes a supercritical liquid. The supercritical CO_2 is slowly vented out of the chamber until the chamber pressure reaches 2.5 MPa, at which point the chamber is cooled and vented quickly to atmosphere since the CO_2 can no longer transition into a liquid.

3.3.5 Fabrication Summary

A brief summary of the fabrication process is shown in the flow chart in Fig. 3.10A), and a scanning electron micrograph of the final result of this fabrication is shown in Fig. 3.10B). The final geometry of the device was measured using a scanning electron microscope (Zeiss Sigma FESEM). When measuring the devices, our accuracy is limited by the size of pixels in the image. We performed all measurements at a magnification of 40000x, where the scale bar of 200 nm is 72 pixels long. This means that each pixel is 2.78 nm long. Rounding up to the nearest nm, this means that we have an uncertainty of ± 3 nm in our measurements. As such, we measured our device to have a waveguide width of 1527 ± 3 nm, the holes of the mirror section had semiaxes $hz = 240 \pm 3$ nm and $hx = 943 \pm 3$ nm, and the center hole had semiaxes $hz = 212 \pm 3$ nm and $hx = 896 \pm 3$ nm.

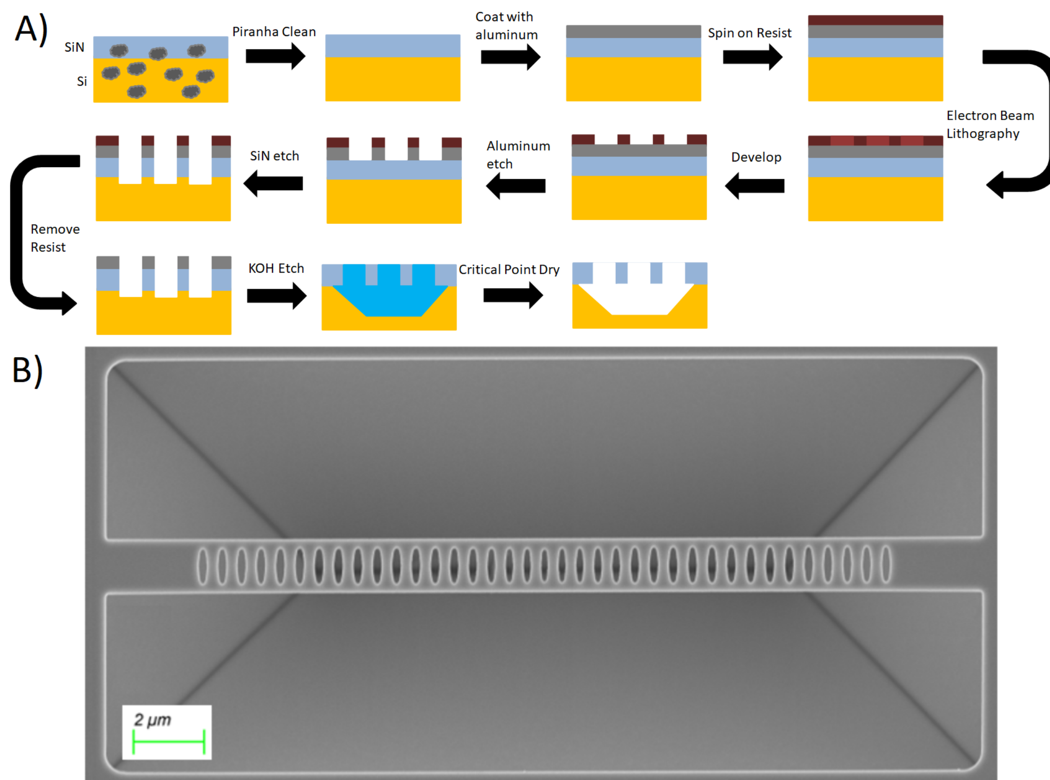

Figure 3.10: A) A flow chart briefly summarizing the steps required for fabricating the OMCs used in this thesis. More details can be found within the text. B) Scanning electron microscope image of one of the OMCs fabricated for this thesis.

Chapter 4

Measurement Techniques

This section discusses the methods used to measure the optical and mechanical characteristics of our OMC. Section 4.1 will cover the optical measurement techniques used, beginning with dimpled-tapered fiber coupling and ending with a discussion on the optical direct detection method. Section 4.2 will discuss methods for performing a phase detection measurement of the mechanical mode. This includes a discussion of the homodyne detection scheme, electrical downmixing of the signal, and how to obtain power spectral densities from the measurement. Lastly, in Section 4.3, we talk about our experimental setup, our procedure for measuring the optical and mechanical modes, our results, and a discussion on how we calculated the optomechanical coupling rate of our system.

4.1 Optical Measurement Techniques

4.1.1 Dimpled-Tapered Fibers

As shown in section 3.2, the optical mode of the OMC primarily exists within the OMC, but some of the field also exists outside the OMC in the form of an evanescently decaying field. Similarly, optical fibers will also have optical modes that evanescently decay away from the fiber. Although the evanescent fields represent the leaking of optical photons into the environment, by overlapping these two evanescent fields we can couple light into and out of the OMC. This is one of the reasons that motivated previous students in the lab to develop a procedure for producing dimpled-tapered fibers. Below I

provide a simplified explanation of how dimpled-tapered fibers are produced, while a more detailed explanation is provided in [57].

Tapered fibers in our lab are generally produced using the heat and pull method [57]. To begin, two fiber patch cords are spliced to the ends of a ∼1 m length of fiber. Both the patch cords and fiber are made from Corning SMF28E+ fiber. In the center of the fiber we strip off ∼2 cm of the cladding where we will be performing the tapering and dimpling procedure. Once the fiber is prepared we connect one patch cord to a laser source and the other to a photodiode, allowing us to monitor the transmission through the fiber throughout the tapering and dimpling procedure. The stripped section of the fiber is placed between two clamps, making sure that the fiber is not twisted and that the clamps are aligned both horizontally and vertically. These clamps are each mounted on linear motorized stages (Zaber T-LSM200A) and, through the use of a computer, provide the pulling force during the tapering procedure.

The stripped section of the fiber is heated through exposure to a hydrogen flame. Note that this does not melt the fiber, but instead softens it, such that when the fiber is pulled the diameter of the fiber will be tapered down. Once the hydrogen flame is in place, the two clamps are slowly pulled apart using the linear motorized stages. Over the course of the pull, the signal amplitude detected on the photodiode will begin to oscillate. The oscillations will increase in frequency until suddenly the oscillations stop. This means that the fiber has become single mode, and serves as a visual indicator of when to stop pulling the fiber and remove the hydrogen flame. A schematic of a tapered fiber is provided in Fig. 4.1A).

Once the fiber is tapered, we also add a dimple to the tapered section of the fiber as shown in Fig. 4.1B). This dimple provides a section of the fiber that is extended away from the rest of the fiber, which is then used as a probe for measuring on-chip devices. The dimple is created by taking a previously tapered section of fiber, lubricating it with graphite, and aligning it perpendicularly with the center of the tapered region. The graphite coated fiber is brought into contact with the tapered fiber, and then lifted while simultaneously loosening the tension in the tapered fiber, resulting in the tapered fiber

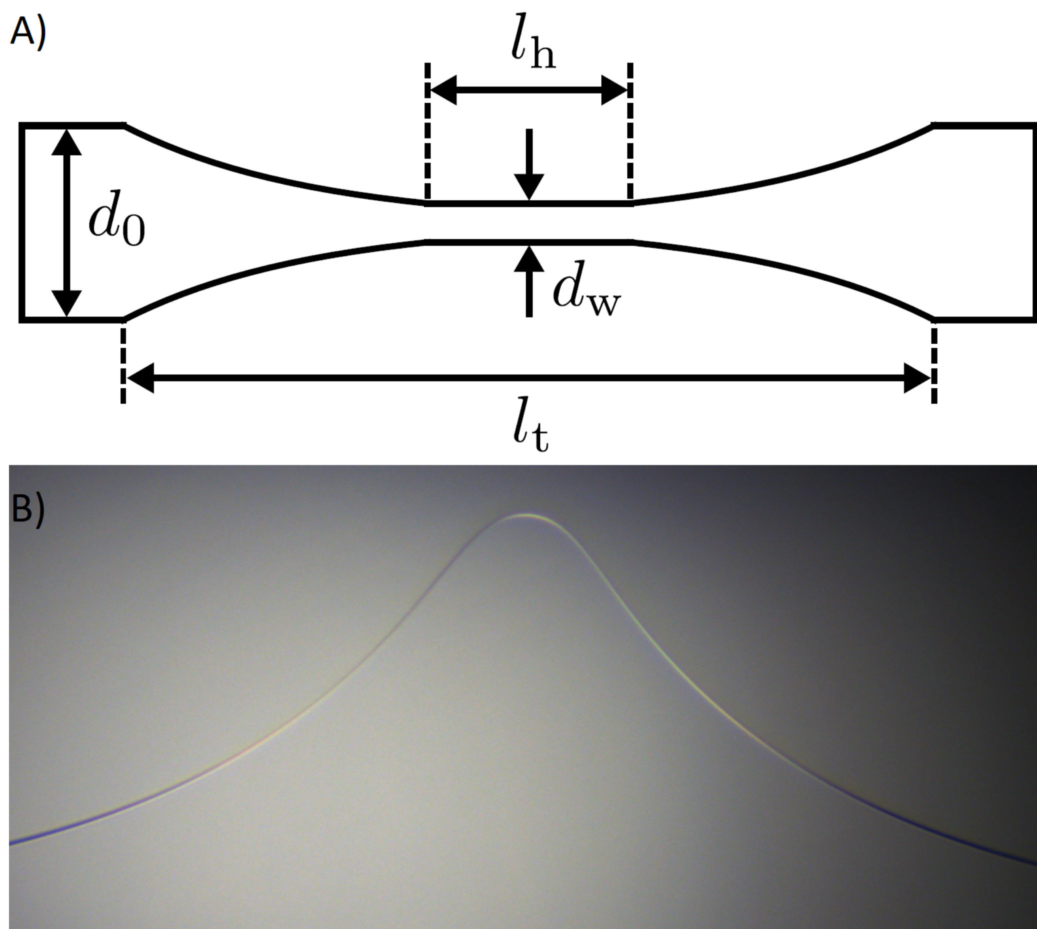

Figure 4.1: A) A Schematic of the fiber after being tapered, adapted from a similar schematic in reference [57]. d_0 is the initial width of the fiber, d_w is the final width of the fiber, l_t is the length of the tapered region, and l_h is the region of fiber exposed to the hydrogen flame. B) Optical microscope image of a completed dimpled-tapered fiber.

wrapping around the graphite coated fiber. We continue to raise and loosen the fibers until the ends of the tapered fiber extend vertically down from the fiber mould. At this point the hydrogen flame is brought back near the fibers for a short moment, annealing the dimple shape into the tapered fiber. The graphite coated fiber can then be lowered, while tightening the tension in the tapered fiber as necessary, until it detaches from the tapered fiber. The two fibers may stick together due to being annealed for too long, but can often be separated by either the flow of hydrogen gas from the unlit hydrogen torch, or by a well placed drop of a solvent such as methanol.

Lastly, the dimpled-tapered fiber is glued to an aluminum mount with two

arms. To secure the fiber to the mount, 5 minute epoxy is deposited on each arm of the mount, and then the mount is raised into the fiber with the dimpled section centered between the arms. The fiber will sink into the epoxy, so it is important to compare the relative heights of the epoxy and the dimple to ensure that the dimple is the highest point. If not, minor adjustments can be made by raising and lowering the clamps holding the fiber. Once properly adjusted, the epoxy is left to harden overnight.

4.1.2 Optical Direct Detection

The optical field of the laser, $\hat{a}_{\text{in}}$, has an intensity given by:

$$|\hat{a}_{\text{in}}|^2 = \frac{P_{\text{l}}}{\hbar\omega_{\text{l}}}, \tag{4.1}$$

where P_{l} is the power of the laser and ω_{l} is the laser frequency [2]. Light scatters away from the fiber at a rate $\kappa = \kappa_0 + \kappa_e$, where the intrinsic scattering rate κ_0 is the rate that light scatters into the environment, while the extrinsic scattering rate κ_e is the rate that light couples into and out of the optomechanical crystal. κ_e depends on the distance between the dimple and the optomechanical crystal and the positioning of the dimple above the optomechanical crystal which allows us to explore three different coupling regimes. When $\kappa_0 > \kappa_e$ we are undercoupled, meaning that cavity losses are dominated by intrinsic losses [2]. When $\kappa_0 < \kappa_e$ we are overcoupled, meaning that some photons are entering and then exiting the cavity before they are able to leak into the environment via intrinsic losses [58]. Lastly, when $\kappa_0 = \kappa_e$ we are critically coupled, meaning photons are entering and exiting the cavity at the same rate [2]. In combination with a three-axis positioning stage, the dimpled tapered fiber provides a convenient platform for coupling light into the optomechanical crystal. An example of what this coupling looks like is shown in the microscope image in Fig. 4.2B).

After interacting with the optical mode of the optomechanical crystal, light couples back into the dimpled fiber at a rate of κ_e. This light is split into two components, the reflected field and the transmitted field. The transmitted

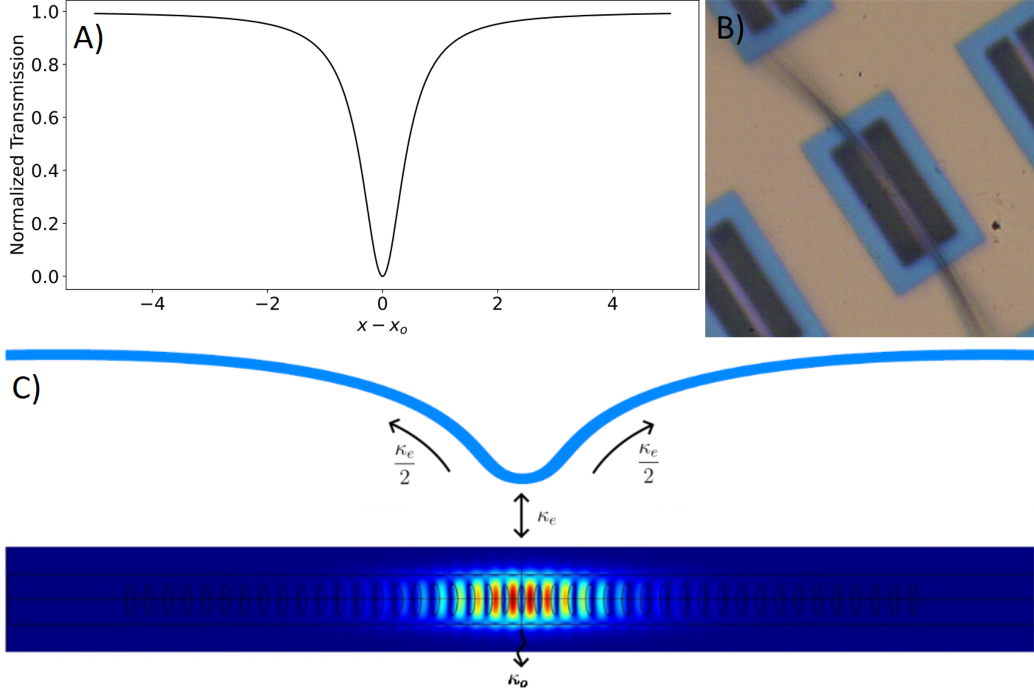

Figure 4.2: A) Example of a Lorentzian shaped transmission dip, such as the ones we expect to observe when measuring the optical resonance of the OMC. The optical resonance is located at the bottom of the Lorentzian, and the total coupling rate is the full-width-half-max of the resonance. B) Microscope image of coupling a dimpled-tapered fiber to an OMC. C) Schematic of how light is coupled into and out of the optomechanical crystal.

optical field can be derived using input-output theory [18] and is given by:

$$\hat{a}_{\text{out}} = \hat{a}_{\text{in}} - \frac{\sqrt{\kappa_e}}{2}\hat{a}. \tag{4.2}$$

The factor of 1/2 in the second term accounts for the reflection losses, which do not reach the photodiode in this measurement scheme. Substituting the steady state solution we derived in Eq. 2.19 into Eq. 4.2, we can obtain the optical intensity detected by the photodiode [18]:

$$\frac{|\hat{a}_{\text{out}}|^2}{|\hat{a}_{\text{in}}|^2} = 1 - (\kappa_0 + \kappa_{\text{e}}/2)\left(\frac{\kappa_{\text{e}}/2}{\Delta^2 + \kappa^2/4}\right), \tag{4.3}$$

where we have normalized the expression by dividing both sides by $|\hat{a}_{\text{in}}|^2$. This expression can be fit to a Lorentzian:

$$y = y_0 - \frac{A}{(x - x_0)^2 + B}, \tag{4.4}$$

allowing for the extraction of key optical parameters: the resonance frequency ω_c, the total decay rate κ, and the quality factor $Q = \omega_c/\kappa$. Additionally, we can calculate the intrinsic and extrinsic scattering rates using the expressions:

$$\kappa_0 = 2\sqrt{B - A}, \tag{4.5}$$

$$\kappa_e = 2\sqrt{B} - 2\sqrt{B - A}, \tag{4.6}$$

where A and B are extracted from the fit. An example Lorentzian is plotted in Fig. 4.2A) to provide an example of what an optical resonance should look like.

4.2 Mechanical Measurement Techniques

Numerous methods exist for measuring the mechanical motion of a resonator, and these can be classified into the two categories of direct detection and phase detection. In all cases, the mechanical signal appears as a modulation of the optical signal, requiring the time-domain signal to be Fourier transformed to obtain information about the mechanical motion [2]. This modulation of the optical mode can be modeled by the expression [18]:

$$\hat{a}(t) = \hat{a}e^{-i\beta_m \sin(\omega_m t)}, \tag{4.7}$$

$$\approx \hat{a}\left[1 - \frac{\beta_m}{2}(e^{i\omega_m t} - e^{-i\omega_m t})\right], \tag{4.8}$$

where ω_m is the frequency of the mechanical signal and:

$$\beta_m = \frac{g_0 x_0}{\omega_m x_{zpf}}, \tag{4.9}$$

is the mechanical modulation index. By inspecting this expression for the modulated optical mode, we can see that applying a modulation like this results in the appearance of two new frequencies, called sidebands, located at $\omega_l + \omega_m$ and $\omega_l - \omega_m$ respectively. Substituting Eq. 4.8 into our expression for the optical output field yields [18]:

$$\hat{a}_{out}(t) = \hat{a}_{in} - \frac{\sqrt{\kappa_e}}{2}\hat{a}\left[1 - \frac{\beta_m}{2}(e^{i\omega_m t} - e^{-i\omega_m t})\right]. \tag{4.10}$$

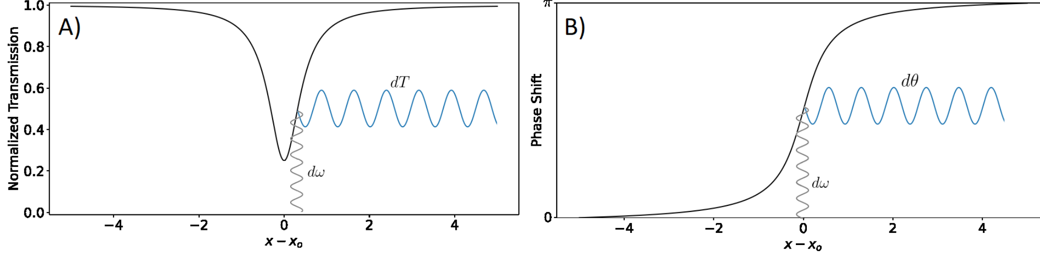

Figure 4.3: A) When the optical mode is modulated by the mechanical signal, it will cause the optical resonance to oscillate back and forth. This $d\omega$ is shown by the gray sinusoid. When doing mechanical direct detection, the laser is detuned from the resonance to the point on the optical resonance with the steepest slope. This translates the change in cavity resonance into a change in transmission detected on the photodiode, dT. The phase of the optical mode is similarly modulated by the mechanical signal, as shown by the grey sinusoid in figure B). In this case, the laser is kept tuned to the optical resonance since this is the point with steepest slope. Information about the mechanical mode is encoded in $d\theta$.

4.2.1 Mechanical Direct Detection

The setup for mechanical direct detection is very similar to what was used for optical direct detection, except instead of sweeping the laser frequency across the optical resonance, we park the laser frequency at one of two points in the optical resonance with the steepest slope. These points can be determined by calculating the zeros of the second derivative of the output optical intensity with respect to the detuning [59]. If our OMC is sideband resolved, $\kappa \ll \omega_{\mathrm{m}}$, the steepest slope for a given ω_{m} appears at the detunings:

$$\Delta = \pm\frac{1}{2}\sqrt{2\omega_{\mathrm{m}}^2 - \kappa^2 - 2\sqrt{\omega_{\mathrm{m}}^4 - 2\kappa^2\omega_{\mathrm{m}}^2}} \approx \pm\frac{\kappa}{2}\left(1 + \frac{\kappa^2}{4\omega_{\mathrm{m}}^2}\right), \tag{4.11}$$

whereas if the OMC is not sideband resolved the steepest slope appears at:

$$\Delta = \pm\frac{1}{6}\sqrt{12\omega_{\mathrm{m}} + 3\kappa^2}. \tag{4.12}$$

At these points we will see a maximum change in signal amplitude when the optical signal is modulated. This scheme is illustrated in Fig. 4.3A).

The AC voltage output by the photodiode is given by [18, 59]:

$$V_{\mathrm{dir}}(t) = \eta_{\mathrm{d}}(\omega)|\hat{a}_{\mathrm{in}}|^2\beta_{\mathrm{m}}\kappa_e K_{dir}(\Delta, \omega_{\mathrm{m}})\sin(\omega_{\mathrm{m}} t), \tag{4.13}$$

where $\eta_{\mathrm{d}}(\omega)$ is the detector efficiency and $K_{dir}(\Delta, \omega_{\mathrm{m}})$ is the transduction function responsible for transducing the cavity resonance frequency fluctuations

into a voltage signal [59]. Both these parameters add gain to the measurement, so they can be treated as fit parameters. Despite its simplicity, this was not the primary method used for measuring mechanical modes in this thesis. More detailed information on direct detection can be found in [59, 60].

4.2.2 Homodyne Detection

When photons enter the OMC they reflect back and forth between the two mirror regions before coupling back into the fiber. These reflections increase the photon path length, equivalent to phase shifting the light that enters the OMC. As such, another way to detect the mechanical motion of the OMC is to measure this phase response. One benefit of measuring the mechanical signal using the phase instead of the intensity is that, as pictured in Fig. 4.3B), the point of steepest slope for the phase response is at a detuning of $\Delta = 0$. Keeping the laser tuned to the optical resonance has the advantage of increasing the number of intracavity photons which, through cavity enhancement, will increase the optomechanical coupling as was discussed in section 1.4.2. Additionally, having $\Delta = 0$ results in a more accurate measurement of the intrinsic mechanical motion since any detuning dependent effects, such as optomechanical backaction [2], are absent.

The phase response of the OMC cannot be measured directly, but instead needs to be measured through interferometry. One such technique is homodyne detection [18] where the light from the laser is split down two arms, the device arm and the local oscillator arm. After the light in the device arm interacts with the OMC, the two arms are recombined at a 50/50 beamsplitter before being detected at a balanced photodiode (BPD). The mixing that occurs at the 50/50 beamsplitter allows the phases of the two arms to be compared, with such differences attributed to mechanical oscillations of the OMC.

Consider a beam splitter with two inputs and two outputs. Following the derivation for the output fields of a beam splitter in reference [61], the beam splitter equation can be described in matrix form as:

$$\begin{bmatrix} E_3 \\ E_4 \end{bmatrix} = \begin{bmatrix} R & T \\ T & R \end{bmatrix} \begin{bmatrix} E_1 \\ E_2 \end{bmatrix}, \tag{4.14}$$

where $R = |R|e^{i\phi_{\mathrm{R}}}$ and $T = |T|e^{i\phi_{\mathrm{T}}}$ are the reflection and transmission coefficients of the beam splitter respectively. Due to conservation of energy, the power in must equal the power out [61]:

$$|E_1|^2 + |E_2|^2 = |E_3|^2 + |E_4|^2, \tag{4.15}$$

which is satisfied for all inputs if:

$$|R|^2 + |T|^2 = 1, \tag{4.16}$$

and:

$$\phi_{\mathrm{R}} - \phi_{\mathrm{T}} = \pm\pi/2. \tag{4.17}$$

The 50/50 beamsplitter is the special case where the reflection and transmission coefficients are equal to $R = 1/\sqrt{2}$ and $T = i/\sqrt{2}$, so our beam splitter equation is given by:

$$\begin{bmatrix} E_3 \\ E_4 \end{bmatrix} = \frac{1}{\sqrt{2}} \begin{bmatrix} 1 & i \\ i & 1 \end{bmatrix} \begin{bmatrix} E_1 \\ E_2 \end{bmatrix}. \tag{4.18}$$

Next, we follow the derivation in reference [58] to determine the intensity detected on the BPD. In the frame rotating with the laser frequency, ω_{l}, the input fields can be described by [58]:

$$a_{\mathrm{LO}}(t) = a_{\mathrm{LO}} e^{i(kz_{\mathrm{LO}} + \phi_{\mathrm{LO}})}, \tag{4.19}$$

and:

$$a_{\mathrm{D}}(t) = a_{\mathrm{D}} e^{i(kz_{\mathrm{D}} + \omega_{\mathrm{m}} t)}, \tag{4.20}$$

where $a_{\mathrm{LO}}(t)$ and $a_{\mathrm{D}}(t)$ correspond to the local oscillator and device arm fields respectively, k is the wavevector of the laser light, and the distance travelled in each arm is given by z_{LO} and z_{D} [58]. The difference in phase between the two arms has been included using the term ϕ_{LO}, which accounts for any time independent phase fluctuations. Inserting these fields into Eq. 4.18 yields:

$$a_1(t) = \frac{1}{\sqrt{2}} \left[a_{\mathrm{LO}} e^{i(kz_{\mathrm{LO}} + \phi_{\mathrm{LO}})} + i a_{\mathrm{D}} e^{i(kz_{\mathrm{D}} + \omega_{\mathrm{m}} t)} \right], \tag{4.21}$$

and:

$$a_2(t) = \frac{1}{\sqrt{2}} \left[a_{\mathrm{D}} e^{i(kz_{\mathrm{D}} + \omega_{\mathrm{m}} t)} + i a_{\mathrm{LO}} e^{i(kz_{\mathrm{LO}} + \phi_{\mathrm{LO}})} \right], \tag{4.22}$$

corresponding to the fields incident on the two ports of the BPD. The ports of the BPD do not measure the amplitude of the optical fields directly, but instead need to be converted to an intensity using the formula $I = \frac{1}{2}\epsilon_0 c|a|^2$. As such, the intensities detected by the ports of the BPD is given by [58]:

$$\begin{aligned} I_{1,2}(t) &= \frac{1}{2}\epsilon_0 c\left[|a_{\mathrm{LO}}|^2 + |a_D|^2 \pm i(a^*_{\mathrm{LO}}a_{\mathrm{D}} - a^*_{\mathrm{D}}a_{\mathrm{LO}})\right], \\ &= \frac{1}{2}\epsilon_0 c\left[|a_{\mathrm{LO}}|^2 + |a_D|^2 \mp 2a_{\mathrm{LO}}a_{\mathrm{D}}\sin(k\Delta z - \phi_{\mathrm{LO}} + \omega_{\mathrm{m}}t)\right], \end{aligned} \tag{4.23}$$

where $\Delta z = z_{\mathrm{D}} - z_{\mathrm{LO}}$ and we assume that the field amplitudes a_{LO} and a_{D} are real. We can simplify this result by taking the difference between the two intensities:

$$I_{\mathrm{B}}(t) = 2a_{\mathrm{LO}}a_{\mathrm{D}}\sin(k\Delta z - \phi_{\mathrm{LO}} + \omega_{\mathrm{m}}t), \tag{4.24}$$

since both intensities contain the same first two terms. In addition to eliminating the large DC terms, this has the benefit of eliminating noise common to both arms. This is one of the reasons that phase detection measurements typically have significantly better signal-to-noise ratios compared to direct detection measurements [58], and is the primary reason why we chose to use the homodyne measurement scheme for measuring the mechanical oscillations of our OMC.

Lastly, in order to isolate the $\omega_{\mathrm{m}}t$ term of the detected intensity we must set up our experiment such that $k\Delta z - \phi_{\mathrm{LO}} = m2\pi$ where $m \in \mathbb{Z}$. If the local oscillator and device arm fields were originally split from the same laser source, we can simply set $\phi_{\mathrm{LO}} = 0$, leaving us with:

$$\Delta z = m\frac{\lambda_0}{n}, \tag{4.25}$$

where we have substituted $k = \frac{2\pi}{(\lambda_0/n)}$ where λ_0 is the wavelength of the laser light in a vacuum and $n \approx 1.47$ is the index of refraction of the fibers used in the interferometer. Even if the path lengths are matched to an integer multiple of the wavelength, it is ideal to minimize m since if m is large, any small shift in the laser wavelength will result in a large phase fluctuation between the interferometer arms. Therefore, it is necessary to match the lengths of the two arms as closely as possible. A detailed procedure for doing this is provided in [18].

Similar to the AC output voltage we found in section 4.2.1, the BPD used here will also have an output voltage given by [18]

$$V_{\text{hom}}(t) = \eta_{\text{d}}(\omega)|a_{\text{LO}}||a_{\text{D}}|\kappa_e\beta_{\text{m}}K_{\text{hom}}(\Delta, \omega_{\text{m}})\sin(\omega_{\text{m}}t) \tag{4.26}$$

where again $\eta_{\text{d}}(\omega)$ and $K_{\text{hom}}(\Delta, \omega_{\text{m}})$ are the detector efficiency and transduction function respectively. In this case, the output voltage depends on both the amplitude of signals in the device arm and local oscillator arm. By using small amplitude signals in the device arm and large amplitude signals in the local oscillator arm, we can perform low-power measurements of the mechanical motion since the signal in the local oscillator arm amplifies the voltage detected on the BPD.

4.2.3 Electrical Downmixing

The range of frequencies that can be measured using homodyne detection is limited by the range of frequencies measurable by our analog to digital converter (ADC). The ADC used in this experiment (Ultradyne AD14-500x2) has a sampling rate of 500 megasamples per second (MS/s), so by Nyquist's theorem [62] which states that you need to sample twice as fast as the highest frequency you want to measure, our ADC can at best measure signals up to 250 MHz. We expect mechanical frequencies on the order of 2.5 GHz, so in order to measure these signals using the equipment we have we need to electrically downmix the signal to below 250 MHz and then digitally upconvert it to the true frequency.

Electrical mixers are much simpler than the mixing that occurs at a 50/50 beamsplitter since in this case the two signals are simply multiplied together [63]. The signal from the BPD, $V_{\text{hom}}(t)$, approximated as:

$$V_{\text{hom}}(t) \approx A_1 \sin(\omega_{\text{m}}t), \tag{4.27}$$

will be multiplied by a local oscillator signal provided by a signal generator:

$$V_{\text{LO}}(t) = A_2 \sin(\omega_{\text{LO}}t), \tag{4.28}$$

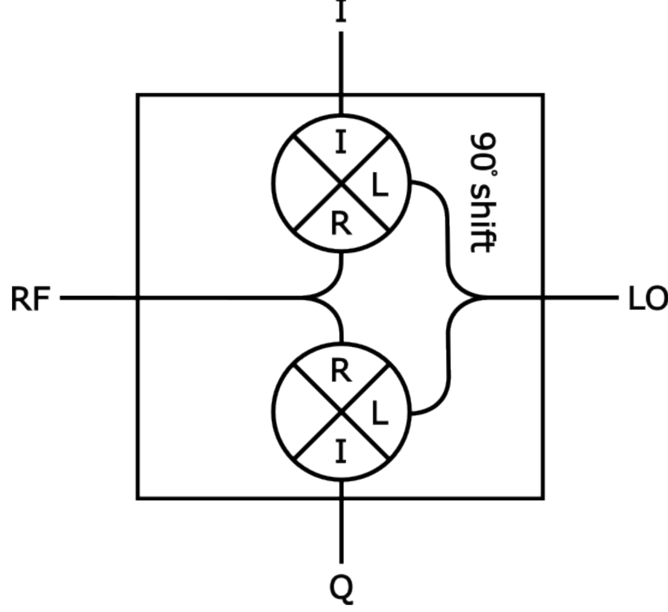

Figure 4.4: A simple schematic of how an IQ mixer works. The RF and LO signals are sent to two mixers, one of which has had the LO signal phase shifted by 90°, allowing access to both quadratures of the mixed signal.

which results in the mixed signal

$$V_{\text{mix}}(t) = \frac{1}{2}A_1A_2\left[\cos(\omega_{\text{m}}t - \omega_{\text{LO}}t) - \cos(\omega_{\text{m}}t + \omega_{\text{LO}}t)\right], \tag{4.29}$$

consisting of two new sinusoids with frequencies which are the sum $\omega_{\text{m}} + \omega_{\text{LO}}$ and difference $\omega_{\text{m}} - \omega_{\text{LO}}$ of the two input frequencies. By choosing an appropriate signal generator frequency, the difference frequency can be downmixed to below 250 MHz while the sum frequency is filtered out. The electrical mixer that was used in these experiments is an IQ mixer (Marki Microwave IQ1545LMP) which has slightly different properties than a standard mixer. An IQ mixer contains two mixers, one of which has had the local oscillator phase shifted by 90°, allowing for separating the in-phase and quadrature signals [63]. The IQ mixer therefore has two output ports, as shown in Fig. 4.4, which will output the signals:

$$I = \frac{A_1A_2}{2}\left[\cos(\omega_{\text{m}}t + \omega_{\text{LO}}t) + \cos(\omega_{\text{m}}t - \omega_{\text{LO}}t)\right], \tag{4.30}$$

$$Q = \frac{A_1A_2}{2}\left[\sin(\omega_{\text{m}}t + \omega_{\text{LO}}t) - \sin(\omega_{\text{m}}t - \omega_{\text{LO}}t)\right]. \tag{4.31}$$

These signals can then be added in quadrature, $I + iQ$, or detected individually depending on what analysis will be performed.

4.2.4 Power Spectral Densities

The voltages described in the previous sections are in the time domain, which when observed directly would appear as a noisy signal oscillating at ω_m. Additionally, due to mechanical damping and the thermal Langevin force [2], the signal's amplitude and phase will randomly fluctuate. In order to obtain useful information about the signal, we need to transform it into the frequency domain. For an arbitrary voltage signal $V(t)$, the Fourier transform over a finite time interval τ is defined as [2]:

$$V(\omega) = \frac{1}{\sqrt{\tau}} \int_0^\tau V(t) e^{i\omega t}.dt \tag{4.32}$$

We include the prefactor $1/\sqrt{\tau}$ to ensures that it is well defined for $\tau \to \infty$. This allows us to determine the noise power spectral density (PSD) $S_{VV}(\omega)$ using the Wiener-Khinchin theorem [2]:

$$\lim_{\tau\to\infty} \langle |V(\omega)|^2 \rangle = S_{VV}(\omega), \tag{4.33}$$

where:

$$S_{VV}(\omega) = \int_{-\infty}^{\infty} \langle V(t)V(0) \rangle e^{i\omega t} dt, \tag{4.34}$$

which contains all the information about mechanical fluctuations in the system. This includes any unwanted background noise in the signal, which fortunately can be separated out from the mechanical signal using the expression [2]:

$$S_{VV}(\omega) = S_{VV}^{w} + \alpha x_\mathrm{zpf}^2 S_{\hat{b}^\dagger \hat{b}}(\omega). \tag{4.35}$$

Assuming that all the technical noise in our system is frequency independent, S_{VV}^{w} encapsulates all background white noise generated by the equipment used while performing the measurement, while $x_\mathrm{zpf}^2 S_{\hat{b}^\dagger \hat{b}^\dagger}(\omega)$ contains all the noise due to mechanical motion which is scaled by the detection factor α. For thermally driven motion, as is the case for all measurements in this thesis, $S_{\hat{b}^\dagger \hat{b}^\dagger}(\omega)$ can be derived directly from the mechanical equation of motion, Eq. 2.51. When $\Delta = 0$, the thermal PSD is given by [18]:

$$S_{\hat{b}^\dagger \hat{b}}^{th}(\omega) = \frac{\Gamma_\mathrm{m} \bar{n}_{th}(\omega_\mathrm{m})}{(\omega_\mathrm{m} + \omega)^2 + \Gamma_\mathrm{m}^2/4}, \tag{4.36}$$

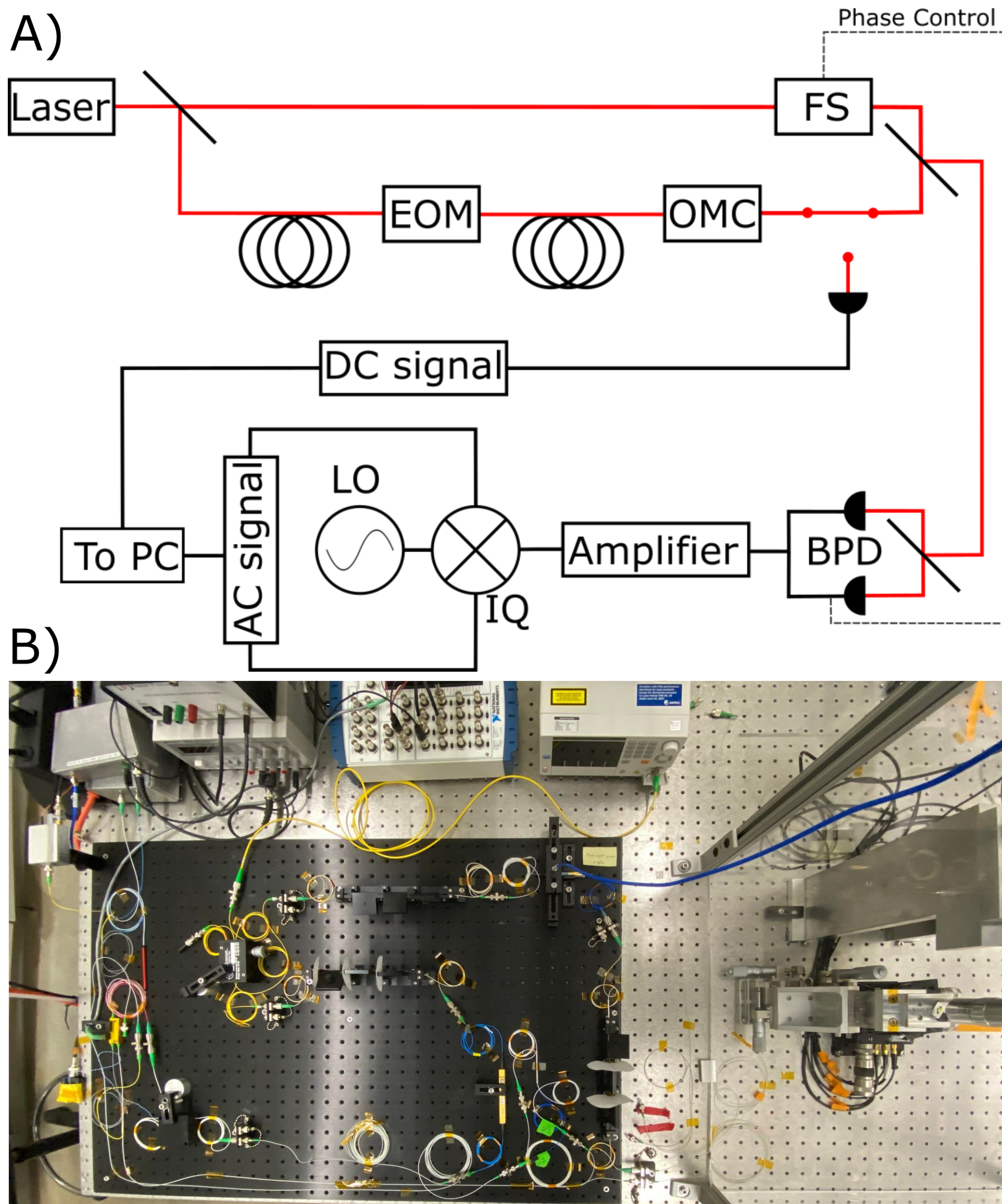

Figure 4.5: A) A schematic of the experimental setup used in this thesis. The optical paths are drawn using a red line while the electronic paths are drawn in black. Beam splitters are denoted using a black line angled at 45°, polarization controllers are denoted using 3 sequential circles, and the optical switch is denoted using three red dots oriented in a triangle. Note that the beam splitter right after the laser is a variable beam splitter, allowing for adjusting the ratio of light in the local oscillator and device arms. The various electronic and optical components are as follows: EOM = electro-optic modulator, FS = fiber stretcher, OMC = optomechanical crystal, BPD = balanced photodiode, IQ = IQ mixer, LO = local oscillator. B) A photo of the fiber setup used in this thesis. Note that an additional polarization controller and EOM have been added to the local oscillator arm, allowing for also doing heterodyne measurements.

where the number of thermal phonons can be calculated using the Bose-Einstein distribution:

$$\bar{n}_{th} = \frac{1}{e^{\hbar\omega_{\mathrm{m}}/k_B T} - 1}. \tag{4.37}$$

4.3 Experimental Setup and Results

All measurements performed in this thesis were done at room temperature. A schematic and a photo of the experimental setup are shown in Fig. 4.5. This setup is equipped with an optical switch, allowing for quickly switching between optical direct detection and homodyne measurement schemes. When doing direct detection the switch is opened, which sends the transmission signal to a single photodiode, while homodyne measurements are done while the switch is closed, which sends the signal to the 50-50 beam splitter where it mixes with the local oscillator before being sent to the BPD.

4.3.1 Optical Mode Characterization

The procedure for measuring the optical mode characteristics is quite simple. As mentioned previously, we will couple light into the OMC using a dimpled-tapered fiber and then measure the transmission on a photodiode. The first step in this measurement is to find the mode of interest, which is done by sweeping the full range of the laser and adjusting the polarization of light that couples to the OMC until we see a dip in transmission. We then narrow the range of the sweep so that it is centered around the mode of interest and adjust the polarization to maximize the depth of the transmission dip.

Once the polarization is properly optimized, we can probe the characteristics of the optical mode by adjusting the coupling distance between the dimpled-tapered fiber and the OMC. When the fiber is far away we are undercoupled, but as the fiber is brought closer we transition to being overcoupled as shown in Fig. 4.6A) and B). Our positioning stage is controlled using the Thorlabs APT model BPC203 peizo controller. This controller comes equipped with an electronic display which, once properly zeroed, shows the approximate lo-

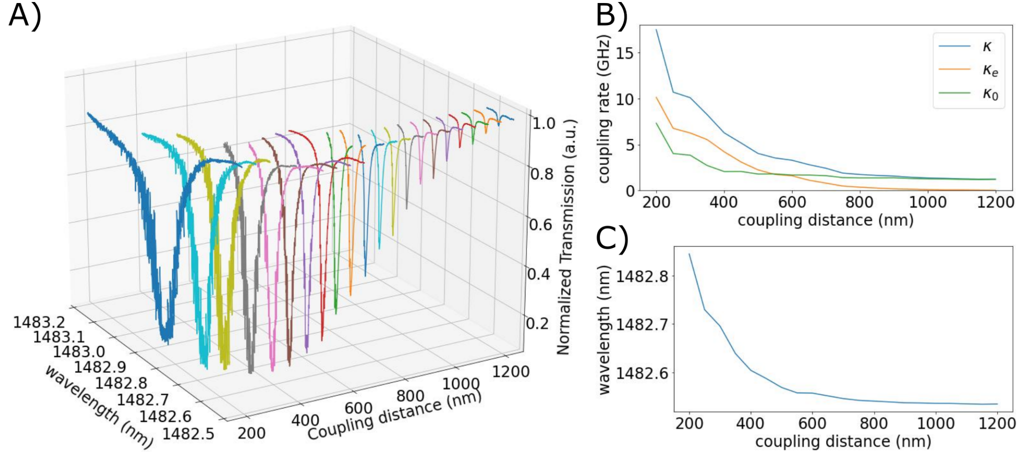

Figure 4.6: A) A plot comparing the coupling distance to the shape of the optical transmission. More details are shown by comparing the coupling distance to B) the total, intrinsic and extrinsic coupling rates, and C) optical resonance wavelength.

cation of the stage in micrometers. For our purposes we set the point at which the fiber touches our chip as our zero point, and measured coupling distances with respect to that.

In Fig. 4.6B) and C) we show how the coupling distance shifts the optical resonance and affects the various coupling rates. Photo-elastic effects due to the high number of cavity photons causes the cavity wavelength to shift from an intrinsic value of $\lambda_c = 1482.55$ nm, to a distorted value of $\lambda_c = 1482.85$ nm at a coupling distance of ≈ 200 nm. Additionally, the OMC has an intrinsic linewidth of $\kappa_0 = 1.19$ GHz, but the proximity of the fiber causes additional photons to scatter out of the OMC, resulting in the intrinsic linewidth increasing [18].

4.3.2 Mechanical Mode Characterization

Due to the narrow 200 MHz search bandwidth imposed by the downmixing scheme, searching for the mechanical resonance signal proved to be the most difficult part of this experiment. A previous member of the group [18] found that the amplitude of the mechanical signal was maximized when $\kappa \approx 5-7$ GHz, so using a coupling distance between 350-450 nm, corresponding to an optical quality factor between 25000-40000, should result in a maximum amplitude of our mechanical signal. We eventually found a mechanical signal

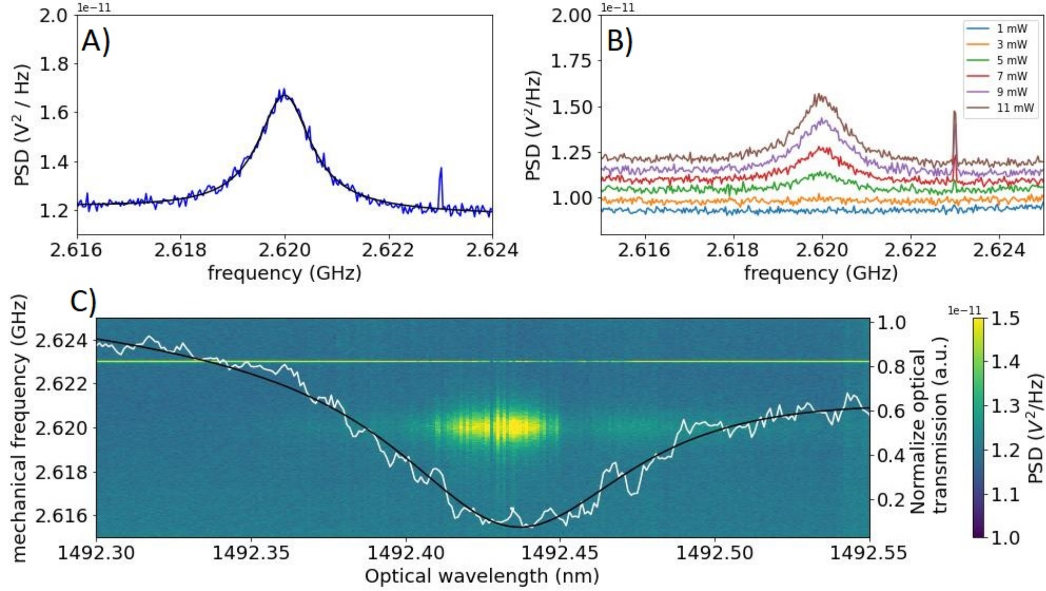

Figure 4.7: A) PSD of the mechanical resonance of our OMC for an input laser power of 10 mW. Also shown here is a fit to the data, from which we obtain $Q_{\mathrm{m}} = 2126$ and $\Gamma_{\mathrm{m}} = 1.23$ MHz. B) PSD for various laser powers, showing the power dependence of our mechanical signal. C) Simultaneous measurement of the mechanical PSD and the optical resonance, showing the relationship between laser wavelength and mechanical signal amplitude.

with a frequency $\omega_{\mathrm{m}} = 2.62$ GHz, but the amplitude of this signal was still quite small. Signal-to-noise was improved by remembering that the amplitude of the optical signal in the local oscillator arm amplifies the mechanical signal at the 50/50 beam splitter. The input beam splitter is variable, allowing tuning of the ratio of light in the local oscillator and device arms. Fig. 4.7A) shows the resulting measurement when the laser is outputting 10 mW and the variable beam splitter is tuned such that 95% of the light goes to the local oscillator arm. The obtained mechanical signal has a mechanical quality factor of $Q_{\mathrm{m}} = 2126$ and a mechanical damping rate of $\Gamma_{\mathrm{m}} = 1.23$ MHz.

Once the mechanical signal has been maximized, there are 2 measurements that must be done to confirm that the signal we are seeing is due to thermomechanical motion. From Eq. 4.26 we note that the voltage detected by the BPD depends on the amplitude of fields in both the device arm and local oscillator arm. Therefore, as shown in Fig. 4.7B), we first verify that the signal we are seeing is due to the mechanical motion of the OMC by sweeping the power of

the laser. When the laser power is low we see no mechanical signal, whereas when the laser power is high we see a well defined mechanical resonance. The second measurement we perform is a laser wavelength sweep to verify that the mechanical signal amplitude is maximized when $\Delta = 0$ and decreases to zero as we tune the laser away from $\Delta = 0$. Referring to Fig. 4.3B), this is because the phase has maximum slope at $\Delta = 0$ and the slope vanishes as we tune the laser away from $\Delta = 0$. This behaviour is confirmed in Fig. 4.7C) where we stepped the laser frequency and measured mechanics at each step. The optical resonance overlaid on top of this plot had an optical quality factor of $Q = 15488$. Due to difficulties with maintaining the position of the fiber throughout the course of this measurement, the quality factor for the optical resonance is outside the ideal range of $Q = 25 - 40\text{k}$. Future implementations of this measurement will use on chip wave guides to optically couple to the OMC, mitigating this problem.

4.3.3 Optomechanical Coupling Rate

The natural next step once we have characterized both the optical mode and mechanical mode is to determine the optomechanical coupling rate. As discussed in section 2.3, the definition of the single-photon optomechanical coupling rate is $g_0 = G x_{\text{zpf}}$ where $G = \frac{d\omega}{dx}$ is the optical frequency shift per displacement [2]. Typically G cannot be measured directly, so instead we implement a technique called thermomechanical calibration [64]. Using the chain rule, the thermomechanically calibrated optomechanical coupling is:

$$g_0 = \frac{d\omega}{dx} x_{\text{zpf}} = \frac{d\omega}{dV_{DC}} \cdot \frac{dV_{AC}}{dx} \cdot x_{\text{zpf}}. \tag{4.38}$$

This equation now has three terms that can be either experimentally measured or calculated numerically. $\sqrt{\alpha} = \frac{dV_{AC}}{dx}$ is a fit parameter of the mechanical power spectrum, $\frac{d\omega}{dV_{DC}}$ can be extracted from the fit of the optical resonance, and m_{eff} can be obtained numerically and inserted into $x_{\text{zpf}} = \sqrt{\frac{\hbar}{2 m_{\text{eff}} \omega_{\text{m}}}}$. Thermomechanical calibration requires precise information of how AC and DC signals are affected by the various electronic and optical components in the system. At low frequency, these components typically contribute very little

noise or gain to the signal, but in the GHz regime their contribution becomes large, leading to inaccurate values of g_0. Since our mechanical resonances are in this GHz regime, we will need to use a different technique to reliably determine g_0.

An alternative way of calculating g_0 is through phase calibration [18]. In addition to the mechanical signal, Fig. 4.7A) and B) shows another narrower peak next to the mechanical signal. This peak is the signal provided by an EOM that is placed in the device arm before the OMC (see Fig. 4.5). Phase calibration compares the mechanical signal of our device to the signal from an EOM with a known driving voltage and frequency near the mechanical frequency [18]. This extra modulation in the signal arm of our homodyne setup can be modeled as a Dirac delta function, leading to a slightly different expression for the PSD:

$$S_{VV}(\omega) = S_{VV}^{w} + \alpha x_{\mathrm{zpf}} S_{\hat{b}^\dagger \hat{b}}(\omega) + S_{VV}^{EOM} \delta(\omega - \omega_{\mathrm{EOM}}), \tag{4.39}$$

where S_{VV}^{EOM} is the amplitude of the modulation provided by the EOM.

The power contained in the two peaks can be determined by calculating the area under the curve. This can be done either by extracting the area from the fit or by numerical integration. For the mechanical signal, the power is given by [18]:

$$P(\omega_{\mathrm{m}}) = \int_{\omega_{\mathrm{m}}} (S_{VV}(\omega) - S_{VV}^{w}) d\omega = \frac{S_{VV}(\omega_{\mathrm{m}})\Gamma_{\mathrm{m}}}{2} = \alpha \beta_{\mathrm{m}}^2, \tag{4.40}$$

while the linewidth of the EOM is typically narrower than the resolution of our Fourier transform so its power needs to be calculated differently. Instead, we can approximate the linewidth from the effective noise bandwidth (ENBW) of the Fourier transform we performed [18]. The ENBW is set by the frequency spacing of points, which can be determined from the ratio:

$$\mathrm{ENBW} = \frac{\mathrm{RATE}}{\mathrm{NFT}}, \tag{4.41}$$

where RATE is the rate at which voltage data is collected, and NFT is the number of points in the Fourier transform. For our Fourier transform, we collected data at a rate of RATE $= 5 \times 10^8$ samples/s and used NFT $= 2^{14}$

points in the Fourier transform, yielding ENBW $\approx$ 30500 Hz. Using this, the power of the EOM peak can be calculated as:

$$P(\omega_{\text{EOM}}) = \int_{\omega_{\text{EOM}}} (S_{VV}(\omega) - S_{VV}^{w}) d\omega = \frac{S_{VV}(\omega_{\text{EOM}}) \cdot \text{ENBW}}{2} = \alpha \beta_{\text{EOM}}^{2}. \tag{4.42}$$

Both the power of the mechanical signal and the power of the EOM signal depend on their respective modulation indices. For the mechanical signal the modulation index, previously defined in Eq. 4.9, is given by:

$$\beta_{\text{m}} = \frac{g_0 x_0}{\omega_{\text{m}} x_{\text{zpf}}}. \tag{4.43}$$

This can be experimentally determined using equipartition theorem [18]. Equipartition theorem relates the average potential energy to the thermal energy of the mechanical mode:

$$\langle U \rangle = \frac{1}{2} m_{\text{eff}} \omega_{\text{m}}^{2} x_0^{2} = \frac{1}{2} k_B T. \tag{4.44}$$

Rearranging the previous two equations with respect to x_0 and solving for β_{m} gives:

$$\beta_{\text{m}} = \sqrt{\frac{2 k_B T}{\hbar \omega_{\text{m}}^{3}}} g_0. \tag{4.45}$$

Rearranging this to solve for g_0, and then inserting the two powers we obtained in Eq. 4.40 and 4.42 we arrive at:

$$g_0 = \sqrt{\frac{\hbar \omega_m^3}{2 k_B T} \beta_{\text{EOM}}^{2} \frac{S_{VV}(\omega_{\text{m}}) \Gamma_{\text{m}}}{S_{VV}(\omega_{\text{EOM}}) \cdot \text{ENBW}}}, \tag{4.46}$$

which can now be determined, assuming we know the modulation index of the EOM.

The modulation index of the EOM can be found by performing a simple calibration of the EOM. To begin, the EOM with modulation index β_{EOM} driven at the frequency ω_{EOM} produces the modulation of the optical field [18]:

$$\hat{a}_{\text{in}}(t) = \hat{a}_{\text{in}} e^{-i \beta_{\text{EOM}} \sin(\omega_{\text{EOM}} t)}. \tag{4.47}$$

For an EOM, the modulation index is defined as $\beta_{\text{EOM}} = \frac{\pi V_{\text{EOM}}}{V_\pi}$ which is the ratio of the EOM driving voltage to the voltage needed to phase shift the light

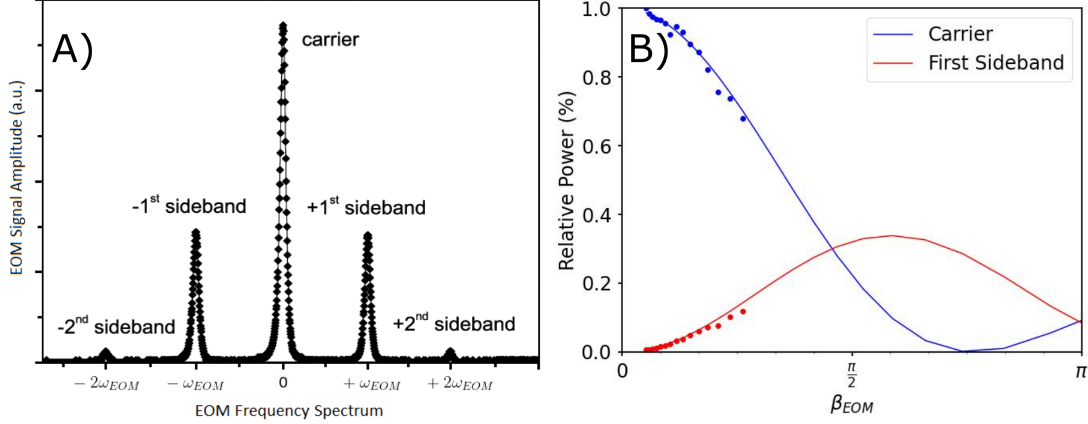

Figure 4.8: A) Example of a frequency spectrum of an EOM. Adapted from a figure taken from [66]. B) The amplitudes of the carrier and first side band of the EOM are fit to the first two squared Bessel functions. The point where $\beta_{\text{EOM}} = \pi$ is used to calibrate the V_π of the EOM.

by π [65]. For small driving voltages this can be simplified by taking the Taylor expansion, but in the case of large driving voltages, as can be the case with EOMs, we instead consider the Jacobi-Anger expansion [18]:

$$e^{-i\beta_{\text{EOM}}\sin(\omega_{\text{EOM}}t)} = -\sum_{n=-\infty}^{\infty} J_n(\beta_{\text{EOM}})e^{in\omega_{\text{EOM}}t}, \tag{4.48}$$

which expresses the field in terms of Bessel functions $J_n(\beta_{\text{EOM}})$. The amplitude of the carrier and sidebands can be fit to the squared values of the corresponding Bessel functions to estimate a value for V_π and therefore an estimate of β_{EOM}.

The amplitudes of the carrier and sidebands can be measured by monitoring the transmission of light through a tunable Fabry Perot cavity as the cavity resonance is swept across the laser frequency [18, 66]. When $V_{\text{EOM}} = 0$, only the carrier will be visible. As shown in Fig. 4.8A), when the applied voltage is increased the sidebands will also appear. The carrier and first sideband amplitudes for various applied voltages, normalized to the maximum carrier amplitude, are plotted and fit to the corresponding squared Bessel functions in Fig. 4.8B). For our EOM we find that the point $\beta_{\text{m}} = \pi$ corresponds to the point when $V_{\text{EOM}} \approx 1.91$ V, which when inserted into the equation for the EOM modulation index allows us to approximate our V_π as $V_\pi \approx 1.91$ V.

Having successfully calibrated the EOM, we can now determine the value of

g_0 for this system. The EOM was driven by a signal generator with $\omega_{\text{EOM}}/2\pi =$ 2.622 GHz and $P_{\text{cal}} = -60$ dBm, resulting in a PSD amplitude of $S_{VV}(\omega_{\text{EOM}}) =$ $1.373e^{-11}$ V^2/Hz. Converting this power to a peak-to-peak voltage yields $V_{pp} =$ $2.236e^{-4}$ V, which can then be substituted into our equation for the EOM modulation index, yielding $\beta_{\text{EOM}} = 0.001$ rad. The mechanical signal occurs at $\omega_{\text{m}}/2\pi = 2.619$ GHz, and from the fit we obtain $S_{VV}(\omega_{\text{m}}) = 1.668e^{-11}\ V^2/Hz$ and $\Gamma_{\text{m}} = 1.232$ MHz. Inserting these values into Eq. 4.46 results in the optomechanical coupling rate

$$g_0/2\pi = 98.7 \text{ kHz}. \tag{4.49}$$

As mentioned in section 2.3.2, this is the rate that energy is transferred between the optical mode and the mechanical mode. As such, this is the main figure of merit for this experiment.

To provide context to this value for the optomechanical coupling rate we can compare this to similar devices made by other research groups. In reference [22] they fabricated a similar device from SiN and measured an optomechanical coupling rate of $g_0/2\pi = 130$ kHz. In reference [31] they fabricated their devices out of diamond and measured $g_0/2\pi = 217$ kHz. This indicates that the devices measured in this thesis have room for improvement. As mentioned in section 3.2.2, the moving boundary optomechanical coupling rate is maximized for small optical mode volumes, large x_{zpf}, and large overlap integrals between the optical and mechanical mode volumes. For the devices measured in this thesis, the mechanical mode volume was calculated to be an order of magnitude larger than the optical mode volume, which we predict contributed to the small value for g_0. In addition to this, the COMSOL simulations predicted a value of $g_{\text{mb}}/2\pi = 348$ Hz, which is significantly smaller than what we measured. Future simulations will need to be performed to find a mechanical mode that better overlaps with the optical mode and which provides a better estimate for the optomechanical coupling rate.

Chapter 5

Conclusion

5.1 Summary

The primary focus of this thesis was the design, fabrication, and measurement of OMCs made from silicon nitride. We began by discussing the theory of optical and mechanical resonators, including the theory for coupled optomechanical systems. Hamiltonians for the optical and mechanical modes were derived using second quantization, then the interaction Hamiltonian was derived as a modulation of the optical mode due to the mechanical motion of the OMC. This method of deriving the interaction Hamiltonian also enabled us to derive the optomechanical coupling strength, one of the main figures of merit for optomechanical systems. Input-output theory was then used to derive the equations of motion that described the optomechanical interaction, as well as accounting for the various ways photons and phonons are coupled into the system or are lost to the surrounding environment.

Following our discussion of optomechanical theory, we described how we designed the OMC in chapter 3. We began by discussing the theory behind OMC band structures, then performed simulations of the mirror and defect unit cells to produce band diagrams of both the optical and mechanical modes. These mirror and defect unit cells were then combined into simulations of both the optical and mechanical modes of the full OMC. Through these simulations we found an OMC geometry that supported a high quality factor optical mode and learned that large spatial overlap between the mechanical and optical modes should result in large optomechanical coupling.

Parameters	Optics	Mechanics
Wavelength/Frequency	$\lambda_c \approx 1482.55 - 1482.85$ nm	$\omega_m/2\pi \approx 2.62$ GHz
Quality Factor	$Q_c \approx 10000 - 160000$	$Q_m \approx 2126$
Total Coupling/Damping Rate	$\kappa_t/2\pi \approx 1.22 - 17.47$ GHz	$\Gamma_m/2\pi \approx 1.23$ MHz
Intrinsic Coupling Rate	$\kappa_0/2\pi \approx 1.21 - 12.40$ GHz	-
Extrinsic Coupling Rate	$\kappa_e/2\pi \approx 0.01 - 5.07$ GHz	-
Optomechanical Coupling Rate	$g_0/2\pi \approx 98.66$ kHz	

Table 5.1: Summary of the optical and mechanical properties of the OMC measured in this thesis

Continuing in chapter 3 we described in detail the fabrication process for making the OMCs. The silicon nitride chips were coated in a thin layer of aluminum, followed by a layer of photoresist. Electron beam lithography was used to transfer the OMC pattern into the photoresist layer, which was then used as a mask for etching the subsequent aluminum and silicon nitride layers. The OMCs were suspended by submerging the chips into a bath of KOH, which selectively etched away the silicon layer below the silicon nitride, before being dried using a critical point dryer.

Lastly, we spent Chapter 4 discussing the various techniques used to measure the OMC. Dimpled tapered fiber couplers were made and used as a probe for coupling light into and out of the OMC. Optical direct detection was used to measure the optical resonance of the OMC, allowing us to relate the distance between the fiber and OMC with changes in the coupling rate and resonant frequency. Once the optical mode was characterized, we used a homodyne detection scheme with electrical downmixing to measure the power spectral density of the mechanical mode. Then, after calibrating the EOM, phase calibration was used to determine the vacuum optomechanical coupling rate of the system. A summary of all the experimental results is provided in Table 5.1.

5.2 Next Steps

As mentioned in section 4.1.2, this system cannot be critically coupled and at best will have $\kappa_e = \kappa_o/2$. This is because half the light that couples from the OMC back into the fiber is lost due to being reflected back down the

fiber towards the laser. To mitigate this, future iterations of the OMC will have light coupled into them using an on chip waveguide. One end of this waveguide will be coupled to a fiber, while the other half will have mirror unit cells patterned into it such that all light will be reflected back to the fiber. Since all light is reflected back down the fiber these devices will need to be measured in reflection, which will require making changes to the experimental setup such as adding a circulator and potentially adding some Fabry-Perot optical filters.

Upon writing this thesis it was discovered that, although the designs we made had great optical properties, the mechanical properties suffered as a result. Future iterations will need to be re-simulated in order to find a geometry that has both good optical and good mechanical properties. This will also present the opportunity to fix the calculation for determining the optomechanical coupling rate since there is a large discrepancy between the simulated and measured results. Fortunately, the simulations performed for this thesis can still be used and will only require slight modifications.

The final goal of these devices is to place them inside a 3D microwave cavity and perform transduction from optical photons to microwave photons, similar to what was done in reference [18]. In this system, the phonons inside the OMC are coupled to the microwave field piezoelectrically, requiring us to switch from using silicon nitride, which is not a piezoelectric material, to lithium niobate, which has great piezoelectric properties. Changing materials will make it necessary to complete new simulations of the OMC, which provides a great opportunity to improve the mechanical characteristics. Once the new simulations are done, there will also need to be some alterations to the fabrication process, since the etch chemistry used for silicon nitride is not compatible with lithium niobate.

Bibliography

[1] A. Einstein, "Zur Quantentheorie der Strahlung", Phys. Z. **18**, 121–128 (1916).

[2] M. Aspelmeyer, T. J. Kippenberg, and F. Marquardt, "Cavity optomechanics", Rev. Mod. Phys. **86**, 1391–1452 (2014).

[3] M. Eichenfield, J. Chan, R. M. Camacho, K. J. Vahala, and O. Painter, "Optomechanical crystals", Nature **462**, 78–82 (2009).

[4] P. J. Winzer, D. T. Neilson, and A. R. Chraplyvy, "Fiber-optic transmission and networking: the previous 20 and the next 20 years [invited]", Opt. Express **26**, 24190–24239 (2018).

[5] M. A. Mohammad, M. Muhammad, S. K. Dew, and M. Stepanova, "Fundamentals of electron beam exposure and development", Nanofabrication, 11–41 (2011).

[6] S. M. Rossnagel, J. J. Cuomo, W. D. Westwood, and G. S. Oehrlein, "Reactive ion etching", in *Handbook of plasma processing technology: fundamentals, etching, deposition, and surface interactions* (Noyes Publ., 1990), 196–232.

[7] J. Z. Buchwald, R. Fox, and A. E. Shapiro, "Newton's optics", in *Oxford handbook of the history of physics* (Oxford University Press, 2013), 166–198.

[8] R. Descartes and N. Poisson, *Discours De La Methode Pour bien conduire sa raison, & chercher la verité dans les Sciences: Plus la Dioptrique, les Meteores, la Mechanique, & la Musique; qui sont des essais de cette Méthode*, v. 2 (Compagnie des Libraires, 1724).

[9] R. Hooke, *Micrographia: or, some physiological descriptions of minute bodies made by magnifying glasses with observations and inquiries thereupon* (Royal Society of London, 1667).

[10] C. Huygens, *Traité de la lumière: où sont expliquées les causes de ce qui luy arrive dans la reflexion, & dans la refraction, et particulièrement dans l'étrange refraction du Cristal d'Islande* (Pierre Vander Aa, 1690).

[11] J. Buchwald, *The Rise of the Wave Theory of Light: Optical Theory and Experiment in the Early Nineteenth Century* (University of Chicago Press, 1989).

[12] M. Planck, "Ueber das gesetz der energieverteilung im normalspectrum", Annalen der Physik **309**, 553–553 (1900).

[13] S. Gröblacher, K. Hammerer, M. R. Vanner, and M. Aspelmeyer, "Observation of strong coupling between a micromechanical resonator and an optical cavity field", Nature **460**, 724–727 (2009).

[14] S. Schreppler, N. Spethmann, N. Brahms, T. Botter, M. Barrios, and D. M. Stamper-Kurn, "Optically measuring force near the standard quantum limit", Science **344**, 1486–1489 (2014).

[15] A. Schliesser, R. Rivière, G. Anetsberger, O. Arcizet, and T. J. Kippenberg, "Resolved-sideband cooling of a micromechanical oscillator", Nature Phys. **4**, 415–419 (2008).

[16] H. Ramp, T. J. Clark, B. D. Hauer, C. Doolin, K. C. Balram, K. Srinivasan, and J. P. Davis, "Wavelength transduction from a 3d microwave cavity to telecom using piezoelectric optomechanical crystals", Appl. Phys. Lett. **116**, 174005 (2020).

[17] S. Krinner, S. Storz, P. Kurpiers, P. Magnard, J. Heinsoo, R. Keller, J. Lütolf, C. Eichler, and A. Wallraff, "Engineering cryogenic setups for 100-qubit scale superconducting circuit systems", EPJ Quantum Technology **6**, `10.1140/epjqt/s40507-019-0072-0` (2019).

[18] H. Ramp, "Microwave to Telecom Wavelength Transduction", PhD thesis (University of Alberta, 2020).

[19] J. Chan, "Laser Cooling of an Optomechanical Crystal Resonator to Its Quantum Ground State of Motion", PhD thesis (California Institute of Technology, 2012).

[20] M. Fox, *Quantum Optics: An Introduction* (OUP Oxford, 2006).

[21] J. Chan, A. H. Safavi-Naeini, J. T. Hill, S. Meenehan, and O. Painter, "Optimized optomechanical crystal cavity with acoustic radiation shield", Appl. Phys. Lett. **101**, 081115 (2012).

[22] M. Davanço, S. Ates, Y. Liu, and K. Srinivasan, "Si_3N_4 optomechanical crystals in the resolved-sideband regime", Appl. Phys. Lett. **104**, 041101 (2014).

[23] T. P. Purdy, K. E. Grutter, K. Srinivasan, and J. M. Taylor, "Quantum correlations from a room-temperature optomechanical cavity", Science **356**, 1265–1268 (2017).

[24] K. C. Balram, M. Davanço, J. Y. Lim, J. D. Song, and K. Srinivasan, "Moving boundary and photoelastic coupling in GaAs optomechanical resonators", Optica **1**, 414 (2014).

[25] M. Forsch, R. Stockill, A. Wallucks, I. Marinković, C. Gärtner, R. A. Norte, F. van Otten, A. Fiore, K. Srinivasan, S. Gröblacher, and et al., "Microwave-to-optics conversion using a mechanical oscillator in its quantum ground state", Nature Phys. **16**, 69–74 (2019).

[26] J. Bochmann, A. Vainsencher, D. D. Awschalom, and A. N. Cleland, "Nanomechanical coupling between microwave and optical photons", Nature Phys. **9**, 712–716 (2013).

[27] A. Vainsencher, K. J. Satzinger, G. A. Peairs, and A. N. Cleland, "Bi-directional conversion between microwave and optical frequencies in a piezoelectric optomechanical device", Appl. Phys. Lett. **109**, 033107 (2016).

[28] L. Fan, X. Sun, C. Xiong, C. Schuck, and H. X. Tang, "Aluminum nitride piezo-acousto-photonic crystal nanocavity with high quality factors", Appl. Phys. Lett. **102**, 153507 (2013).

[29] R. Stockill, M. Forsch, G. Beaudoin, K. Pantzas, I. Sagnes, R. Braive, and S. Gröblacher, "Gallium phosphide as a piezoelectric platform for quantum optomechanics", Phys. Rev. Lett. **123**, 163602 (2019).

[30] K. Schneider, Y. Baumgartner, S. Hönl, P. Welter, H. Hahn, D. J. Wilson, L. Czornomaz, and P. Seidler, "Optomechanics with one-dimensional gallium phosphide photonic crystal cavities", Optica **6**, 577–584 (2019).

[31] M. J. Burek, J. D. Cohen, S. M. Meenehan, N. El-Sawah, C. Chia, T. Ruelle, S. Meesala, J. Rochman, H. A. Atikian, M. Markham, D. J. Twitchen, M. D. Lukin, O. Painter, and M. Lončar, "Diamond optomechanical crystals", Optica **3**, 1404 (2016).

[32] J. V. Cady, O. Michel, K. W. Lee, R. N. Patel, C. J. Sarabalis, A. H. Safavi-Naeini, and A. C. Bleszynski Jayich, "Diamond optomechanical crystals with embedded nitrogen-vacancy centers", Quantum Sci. Technol. **4**, 024009 (2019).

[33] M. Mitchell, D. P. Lake, and P. E. Barclay, "Optomechanically amplified wavelength conversion in diamond microcavities", Optica **6**, 832 (2019).

[34] W. Jiang, R. N. Patel, F. M. Mayor, T. P. McKenna, P. Arrangoiz-Arriola, C. J. Sarabalis, J. D. Witmer, R. Van Laer, and A. H. Safavi-Naeini, "Lithium niobate piezo-optomechanical crystals", Optica **6**, 845 (2019).

[35] W. Jiang, C. J. Sarabalis, Y. D. Dahmani, R. N. Patel, F. M. Mayor, T. P. McKenna, R. Van Laer, and A. H. Safavi-Naeini, "Efficient bidirectional piezo-optomechanical transduction between microwave and optical frequency", Nat. Commun. **11**, 1166 (2020).

[36] *LPCVD Silicon Nitride (Stoichiometric)*, Accessed: 2022-12-05.

[37] *Silicon Nitride*, Accessed: 2022-12-05.

[38] C. Reinhardt, T. Müller, A. Bourassa, and J. C. Sankey, "Ultralow-noise sin trampoline resonators for sensing and optomechanics", Phys. Rev. X **6**, 021001 (2016).

[39] R. A. Norte, J. P. Moura, and S. Gröblacher, "Mechanical resonators for quantum optomechanics experiments at room temperature", Phys. Rev. Lett. **116**, 147202 (2016).

[40] C. Doolin, "Integrated Optical and Mechanical Resonators for Evanescent Field Sensing", PhD thesis (University of Alberta, 2019).

[41] J. D. Joannopoulos, S. G. Johnson, and J. N. Winn, *Photonic crystals: Molding the flow of light - second edition* (Princeton University Press, 2011).

[42] P. Mackenzie-Helnwein, "Some remarks on the compressed matrix representation of symmetric second-order and fourth-order tensors. comput. methods appl. mech. eng. 190(22-23), 2753-2770", Comput. Method Appl. Mech. Eng. **190**, 2753–2770 (2001).

[43] Z.-G. Huang, "Analysis of acoustic wave in homogeneous and inhomogeneous media using finite element method", in *Acoustic waves*, edited by M. G. Beghi (IntechOpen, Rijeka, 2011) Chap. 1.

[44] COMSOL Multiphysics® v. 6.0, *www.comsol.com*, COMSOL AB, Stockholm, Sweden.

[45] *MATLAB version 9.12.0.2039608 (R2022a)*, The Mathworks, Inc. (Natick, Massachusetts, 2022).

[46] B. Hauer, "On-Chip Silicon Optomechanical Cavities at Low Temperatures", PhD thesis (University of Alberta, 2019).

[47] *Fabrication and Characterization Facility*, Accessed: 2022-12-05.

[48] A. Hryciw, personal communication, Sept. 22, 2021.

[49] T. Okada, J. Fujimori, M. Aida, M. Fujimura, T. Yoshizawa, M. Katsumura, and T. Iida, "Enhanced resolution and groove-width simulation in cold development of zep520a", Journal of Vacuum Science & Technology B **29**, `10.1116/1.3569892` (2011).

[50] E. Zohari, personal communication, Nov. 4, 2021.

[51] M. Wasilik and N. Chen, "Deep reactive ion etch conditioning recipe", in Micromachining and microfabrication process technology ix, Vol. 5342, edited by M. A. Maher and J. F. Jakubczak (International Society for Optics and Photonics, 2003), pp. 103–110.

[52] P. Ehrburger, P. Baranne, and J. Lahaye, "Inhibition of the oxidation of carboncarbon composite by boron oxide", Carbon **24**, 495–499 (1986).

[53] M. Hume and G. d. O. Luiz, *Koh etching of Bulk Silicon*, Accessed: 2022-12-05.

[54] A. Witkowski, M. Majkut, and S. Rulik, "Analysis of pipeline transportation systems for carbon dioxide sequestration", Archives of Thermodynamics **35**, 117–140 (2014).

[55] D. Sanli, S. Bozbağ, and C. Erkey, "Synthesis of nanostructured materials using supercritical CO_2 : part i. physical transformations", J. Mater. Sci. **47**, 2995–3025 (2011).

[56] S. Munro and A. Hryciw, *Critical point drier sop*, Accessed: 2022-12-05.

[57] B. D. Hauer, P. H. Kim, C. Doolin, A. J. MacDonald, H. Ramp, and J. P. Davis, "On-chip cavity optomechanical coupling", EPJ Techn Instrum **1**, 4 (2014).

[58] A. MacDonald, "Cryogenic Optomechanics with Silica Microresonators", MA thesis (University of Alberta, 2015).

[59] M. L. Gorodetsky, A. Schliesser, G. Anetsberger, S. Deleglise, and T. J. Kippenberg, "Determination of the vacuum optomechanical coupling rate using frequency noise calibration", Opt. Express **18**, 23236 (2010).

[60] A. J. MacDonald, G. G. Popowich, B. D. Hauer, P. H. Kim, A. Fredrick, X. Rojas, and J. P. Doolin P. nd Davis, "Optical microscope and tapered fiber coupling apparatus for a dilution refrigerator", Review of Scientific Instruments **86**, 013107 (2015).

[61] R. Loudon, "Classical theory of optical fluctuations and coherence", in *The quantum theory of light* (Oxford University Press, 2010), 82–124.

[62] C. Shannon, "Communication in the presence of noise", Proceedings of the IRE **37**, 10–21 (1949).

[63] D. Jorgesen, *The why and when of IQ Mixers for Beginners*, Accessed: 2022-12-05.

[64] B. Hauer, C. Doolin, K. Beach, and J. Davis, "A general procedure for thermomechanical calibration of nano/micro-mechanical resonators", Annals of Physics **339**, 181–207 (2013).

[65] *Lithium niobate electro-optic modulators, fiber-coupled (1260 NM - 1625 nm)*, Accessed: 2022-12-05.

[66] I. Dotsenko, "Raman spectroscopy of single atoms", MA thesis (Bonn University, 2002).